

PSFC/JA-05-37

Impurity Transport in Alcator C-Mod Plasmas

Rice, J.E., Terry, J. L., Marmor, E. S., Granetz, R. S. Greenwald,
M. J., Hubbard, A. E., Irby, J. H., Pedersen T. Sunn, Wolfe, S. M.

**Plasma Science and Fusion Center
Massachusetts Institute of Technology
Cambridge MA 02139 USA**

This work was supported by the U.S. Department of Energy, Grant No. DE-FC02-99ER54512. Reproduction, translation, publication, use and disposal, in whole or in part, by or for the United States government is permitted.

Impurity Transport in Alcator C-Mod Plasmas

J. E. Rice, J. L. Terry, E. S. Marmor, R. S. Granetz,
M. J. Greenwald, A. E. Hubbard, J. H. Irby, T. Sunn Pedersen[†] and S. M. Wolfe

Plasma Science and Fusion Center, MIT, Cambridge, MA 02139-4307

[†]*Columbia University*

Abstract

Trace non-recycling impurities (Sc and CaF₂) have been injected into Alcator C-Mod plasmas in order to determine impurity transport coefficient profiles in a number of operating regimes. Recycling Ar has also been injected to characterize steady state impurity density profiles. Subsequent impurity emission has been observed with spatially scanning x-ray and VUV spectrometer systems, in addition to very high spatial resolution x-ray and bolometer arrays viewing the plasma edge. Measured time-resolved brightness profiles of helium-, lithium- and beryllium-like transitions have been compared with those calculated from a transport code which includes impurity diffusion and convection, in conjunction with an atomic physics package for individual line emission. Similar modeling has been performed for the edge observations, which are unresolved in energy. The line time histories and the profile shapes put large constraints on the impurity diffusion coefficient and convection velocity profiles. In L-mode plasmas, impurity confinement times are short (~ 20 ms), with diffusivities in the range of 0.5 m²/s, anomalously large compared to neo-classical values. During EDA H-modes, the impurity confinement times are longer than in L-mode plasmas, and the modeling suggests that there exists inward convection (≤ 50 m/s) near the plasma edge, with greatly reduced diffusion (of order 0.1 m²/s), also in the region of the edge transport barrier. These edge values of the transport coefficients during EDA H-mode are qualitatively similar to the neo-classical values. In ELM-free H-mode discharges, impurity accumulation occurs, dominated by large inward impurity convection in the pedestal region. A scaling

of the impurity confinement time with H-factor reveals a very strong exponential dependence. In ITB discharges, there is significant impurity accumulation inside of the barrier foot, typically at $r/a = 0.5$. Steady state impurity density profiles in L-mode plasmas have a large up-down asymmetry near the last closed flux surface. The impurity density enhancement, in the direction opposite to the ion $\mathbf{B} \times \nabla \mathbf{B}$ drift, is consistent with modeling of neo-classical parallel impurity transport.

I. Introduction

Impurities can play a significant role in fusion plasma performance through radiation losses and dilution of fuel in the plasma core [1,2], so it is important to understand the impurity sources and subsequent transport into the plasma [3]. The employment of injected non-intrinsic, non-recycling impurities allows for the isolation and study of impurity transport [4]. In L-mode plasmas, the impurity confinement is generally found to be short [5-9], with the impurity diffusion anomalously large compared to neo-classical predictions, and intrinsic impurity radiation is not a dominant participant in the overall energy balance. However, in enhanced energy confinement H-mode plasmas, impurity confinement can be very long [10-16] and play an important role in the energy balance. Of particular concern is the core impurity accumulation observed in discharges with internal transport barriers (ITBs) [17-19].

For Alcator C-Mod, the impurity transport coefficient profiles have been determined for L-mode, EDA H-mode, ELM-free H-mode and ITB plasmas. In Sec. II the impurity injection experiments are described. In Secs. III, IV and V, the determination of the impurity transport coefficient profiles is presented for L-mode, H-mode and ITB plasmas, respectively. In Sec. VI, observations of parallel impurity transport are shown, with a summary and conclusions in Sec. VII.

II. Experiment and Spectrometer Description

Scandium and calcium fluoride (CaF_2) have been injected into L- and H-mode plasmas using the laser blow-off technique [4], while argon was introduced through a piezo-electric valve. Subsequent x-ray emission was recorded by a spatially scanable x-ray spectrometer array [20], each spectrometer of which has a resolving power of 5000, a 2 cm spatial resolution and a luminosity function of $7 \times 10^{-9} \text{ cm}^2\text{-sr}$, with spectra typically collected every 20 ms, and with 120 mÅ coverage. The total count rate within the spectral range of the spectrometers ($2.7 \text{ \AA} < \lambda < 4 \text{ \AA}$) is available

with 1 ms time resolution. In most of the analysis presented here, the resonance line, w, ($1s2p\ ^1P_1 - 1s^2\ ^1S_0$) of helium-like ions has been used; for Sc^{19+} , Ca^{18+} and Ar^{16+} , the transitions are at 2.8731 Å [21], 3.1773 Å [22,15] and 3.9492 Å [22,23], respectively. For the VUV emission, an absolute-intensity-calibrated spatially scanning VUV spectrograph [24] has been employed to monitor the brightness of the $1s^22s - 1s^22p$ transitions in the lithium-like ions Sc^{18+} at 279.8 Å and Ca^{17+} at 344.8 Å (the brighter transition of the Li-like calcium doublet at 302.2 Å is contaminated by the intense helium Ly_α line at 303.8 Å), the $1s^22s^2 - 1s^22s2p$ transition of beryllium-like Ca^{16+} at 192.9 Å, the sodium-like Ca^{9+} $3s-3p$ doublet at 557.8 and 574.0 Å and the lithium-like F^{6+} $2s-2p$ doublet at 883.1 and 890.8 Å. This VUV spectrometer has ~ 0.6 Å 1^{st} order spectral resolution and 2 cm spatial resolution, with spectra collected typically every 4 - 16 ms. Both spectrometer systems can view all of the plasma, out to the last closed flux surface. These spectrally resolved measurements are nicely complemented by high spatial resolution observations of the plasma edge (in the vicinity of the transport barrier) from x-ray and bolometer arrays, which are described in Chapter XVIII on diagnostics.

The impurity transport coefficients $D(r)$ and $V(r)$ have been determined from the time evolution of the radial brightness profiles of the helium-, lithium- and beryllium-like x-ray and VUV transitions of injected impurities, and from the profile evolutions of (unresolved in energy) x-ray and bolometer emissivities. The simulated time histories were determined by the following method: the individual charge state density profile time evolutions were determined from the MIST code [25], which uses measured electron density and temperature profiles as inputs, and the impurity diffusion coefficient and convection velocity profiles were taken as free parameters, constant in time. The emissivity profiles for individual transitions were then calculated from the LINEST code [26] using the appropriate population rate coefficients [27-31] in conjunction with the calculated charge state density profiles, along with the measured electron density and temperature profiles. The chordal line brightness time histories for the individual transitions were then determined by integrating the emissivity profiles over the appropriate sight lines. The absolute

impurity densities may be determined by comparing the calculated signals with the observed line brightnesses. The spatial variations, time histories and relative intensities of these profiles place a very strong constraint on the selection of the transport coefficient profiles.

III. Impurity Transport in L-mode Plasmas

Shown in Fig.1 are parameter time histories for an L-mode plasma into which a trace amount of scandium was injected. For the case of L-mode plasmas, the impurity confinement times are short, nominally around 20 ms. An example of the time histories of central chord helium- (dots) and lithium-like (asterisks) scandium brightnesses [14] from another L-mode discharge is shown in Fig.2. The radiation from the two charge states (the x-ray signal has been increased by a factor of 100 for easier direct comparison) peaks sequentially in time, and the scandium has totally left the plasma within 100 ms after the injection. For this particular discharge, at the time of injection (0.75 s), the plasma current was 1.2 MA, the toroidal magnetic field was 7.9 T, the central electron density was $2.0 \times 10^{20}/\text{m}^3$, the central electron temperature was 2800 eV, and there were 1.0 MW of auxiliary Ion Cyclotron Range of Frequencies (ICRF) heating power. For most Alcator C-Mod electron temperature profiles, helium-like scandium is a central charge state, while lithium-like radiates mostly from the outer third of the plasma. Also shown in the figure by the curves are the simulated central chord brightness time histories, calculated as described above. Not only is the agreement between the time histories of the measured and calculated lines quite good, but the relative intensities of the simulated and observed lines are also excellent. Here, there was only one normalization used (of the VUV line), which determines the scandium density in the plasma at one time. The impurity diffusion coefficient profile used for these simulations, along with the electron density and temperature profiles, are shown in Fig.3. The diffusion coefficient was $0.5 \text{ m}^2/\text{s}$ over most of the plasma interior, and then dropped to about $0.05 \text{ m}^2/\text{s}$ near the last closed flux surface at $r = 0.22 \text{ m}$; there was no

need for any convection velocity in this simulation, similar to what was found in Alcator A and C [5,7]. Inclusion of any inward convection velocity would cause the predicted Li-like scandium signal to increase much more quickly than is observed; effects on the predicted He-like signal in this case would be insignificant.

Shown in Fig.4 are the time histories from three x-ray spectrometer views of a Sc injection into another L-mode plasma, integrated over the wavelength region between 2.86 and 2.94 Å. In this case the scandium injection time was 0.550 s. The three traces were from spectrometers viewing at $r/a = 0.10$, 0.39 and 0.69, respectively. The signals all decay with a $1/e$ time of about 19 ms, which implies a diffusion coefficient of about $0.5 \text{ m}^2/\text{s}$, as determined above. Notice that the signal at $r/a = 0.39$ (middle) rises to a peak in about 5 ms, nearly a factor of 2 faster than the more central chord (top) [21]. The transition upper level population at these radii is dominated by collisional excitation of helium-like scandium, which exists over most of the plasma. During the influx phase of the injection, it takes longer for the scandium to reach the plasma center, so the signal at $r/a = 0.10$ peaks later than the signal at $r/a = 0.39$. In contrast, the outermost signal from $r/a = 0.69$ (bottom) actually peaks later than that of the central chord. This is because, in the outer plasma regions where the electron temperature is much less than the transition energy, the upper levels for the lines are mainly populated by radiative recombination of hydrogen-like Sc^{20+} and during the influx phase of the injection, there is no hydrogen-like scandium at this radius. So it is only late in the injection after Sc^{20+} is born at the center of the discharge and then diffuses out to this radius that the signal appears. At $r/a = 0.9$, the electron temperature was $\sim 600 \text{ eV}$; here at 2 ms after the injection, the ion density ratio of $\text{Sc}^{20+}/\text{Sc}^{19+}$ was 10^{-5} , whereas at 15 ms after the injection, the ratio was 0.005. Also shown (by the smooth curves) are the code results, which are in excellent agreement. This agreement is taken to validate the use of the L-mode diffusion coefficient profile of Fig.3.

IV. Impurity Transport in H-mode Plasmas

Impurity confinement times are considerably longer in H-mode discharges [14,15]. The time histories of several parameters of interest for an EDA H-mode plasma are shown in Fig.5. The EDA H-mode period for this 5.4 T deuterium discharge, induced by 2.0 MW of ICRF power, lasted from 0.63 to 1.21 s, as evidenced by increases in the plasma stored energy, the electron density and the electron and ion temperatures. (The steady EDA interval was from 0.7 to 1.2 s.) The stored energy increase during the H-mode period was a modest 40 kJ, and the ITER-89P H-factor was 1.2. There was a CaF₂ injection at 0.8 s, as seen by the increases in the soft x-ray signal and the total calcium density. Shown in Fig.6 is the time evolution of the Ca¹⁸⁺ x-ray spectrum between 3.17 and 3.22 Å for this same EDA H-mode plasma. The spectrum is dominated by the resonance line and the forbidden line, z , ($1s2s\ ^3S_1 - 1s^2\ ^1S_0$, 3.2111 Å), and the intercombination lines are prominent. Also visible are several dielectronic and inner shell satellites. This spectrum is described in detail in Ref.[32]. For this central chord view, all of the individual transitions rise and fall with similar time signatures. Shown in the top frame of Fig.7 is the time history of the brightest x-ray transition, the resonance line, w , from Ca¹⁸⁺ for the same EDA H-mode discharge of Fig.5. The signal reaches a maximum about 35 ms after the injection, and then decays with a characteristic time of 68 ms, which is indicative of the central impurity confinement time. Also shown in the top frame are the time histories of the Li- and Be-like resonance lines, which peak much more quickly but have similar decay times. In the bottom frame of the figure are the simulated normalized brightness time histories, which are in good agreement with the observations. The transport coefficient profiles, near the plasma edge, used in the simulations of Fig.7 are shown in Fig.8 by the solid lines, along with the edge electron density and temperature profiles. Over the plasma core region, the diffusion coefficient is about a factor of two lower than the case of L-mode, which was shown in Fig.3. Plotted for comparison are the calculated neo-classical impurity transport coefficient [33] profile. A more recent treatment of neo-classical impurity transport coefficients may be found in Ref.[34]. In the region of the edge pedestal and transport barrier, the diffusion coefficient profile (0.15 m²/s) is very similar to

the calculated neo-classical profile [14], while in the interior of the plasma the diffusion is highly anomalous, much larger than neo-classical. The convection velocity profile is qualitatively very similar to the calculated neo-classical profile, with the inward pinch the strongest where the density gradient is the largest, and near 0 elsewhere. The peak value for the observed pinch is -70 m/s, a factor of 5 smaller than the neo-classical value. The position of the last closed flux surface is indicated by the vertical dotted line.

By scanning the x-ray and VUV spectrometers shot-to-shot, complete brightness profiles of selected lines may be obtained. Two such brightness profiles are shown in Fig.9, for the Ca^{18+} resonance line (3.1773 \AA) at 0.870 s and for the Ca^{16+} resonance line (192.9 \AA) at 0.815 s, from a series of discharges identical to that shown in Fig.5. The Ca^{18+} resonance line profile is sharply peaked near the plasma center since the dominant population mechanism for the upper level of this transition is collisional excitation, and here the electron temperature is highest. The Ca^{16+} resonance line brightness profile is strongest in the outer regions of the plasma since this is where that charge state density profile is peaked. Shown for comparison are the simulated profiles, using the same transport coefficient profiles from Fig.8, again with good agreement. From Figs.7 and 9 it can be seen that one set of impurity transport coefficients produces good agreement with both the temporal and spatial variations of individual calcium line brightnesses over the complete plasma cross section. Another way of visualizing this is *via* contour plots of line brightness profiles. Shown in Figs.10 and 11 are plots of the measured He- and Be-like transitions, respectively, including the simulated contours. Again, the overall agreement is good.

The details of the transport coefficient profiles in the vicinity of the edge transport barrier may be revealed through use of the complement high spatial resolution edge diagnostics available on Alcator C-Mod. The measured x-ray emissivity profile at the peak of the injection in the neighborhood of the last closed flux surface (LCFS), with the pre-injection background subtracted off, is shown in Fig.12, for the same discharge conditions as in Figs.5-7 and 9-11. This emission is mainly due

to F^{8+} . The x-ray ‘pedestal’ is located well inside of the LCFS and the measured electron density pedestal (top frame), which clearly demonstrates the effect of the inward impurity pinch [15,16]. Also shown in the figure is the simulated x-ray emissivity profile, again using the transport coefficient profiles of Fig.8, which is in excellent agreement with the observed profile. The simulated emission is modeled with all of the fluorine radiation which can contribute within the band pass of the Be foil on front of the detector, the Rydberg series of F^{8+} and F^{7+} and the radiative recombination continuum from fully stripped F^{9+} . 50 % of the total radiation however is from F^{8+} Ly_{α} and Ly_{β} . The match between the measured and simulated profile (location of the x-ray pedestal) puts very large constraints on the location of the inward convection velocity pinch, and on the relative magnitudes of D and V at that location [16].

For the case of ELM-free H-modes, the impurity confinement times are even longer than in EDA H-mode plasmas, and the transport is so slow that the impurity signals don’t reach a peak during the ELM-free period [14], as demonstrated in Fig.13. The ELM-free period began at 0.6 s shortly after the ICRF power was turned on, and the scandium was injected at 0.7 s. The Sc^{18+} brightness increased steadily following the injection, and began to decay at 0.86 s when the ELM-free period ended, as seen on the D_{α} signal. The total radiated power also increased steadily during this time, until the radiation dominated the input power, causing the stored energy to drop. During the subsequent EDA H-mode (0.86 - 1.04 s), the impurity confinement time was reduced to ~ 100 ms, as reflected in the decay of the scandium signal, and the radiated power decreased as well, allowing the stored energy to rise again. The ICRF heating power was turned off at 1.04 s, and the plasma reentered L-mode at 1.135 s, when the scandium decayed with a confinement time of around 20 ms, the nominal L-mode value. The scandium remained in the plasma for 500 ms. During the ELM-free period, the impurity transport coefficient profiles are qualitatively similar to those in the EDA case, but quantitatively, the convection velocity reaches more negative values, close to the neo-classical levels [14,15]. Such impurity transport coefficients lead to very long impurity confinement

(> 1 s) and this is why the VUV signal in Fig.13 was unable to reach a peak and begin to decay before the plasma went out of ELM-free H-mode.

There is a very strong dependence of the impurity confinement time on the energy confinement H-factor, as shown in Fig.14. There is a cluster of points between 0.8 and 1.0 for L-mode plasmas, with impurity confinement times in the range from 15-30 ms, and another cluster for EDA H-mode plasmas with an H-factor between 1.2 and 1.5. For these latter plasmas, the impurity confinement times are in the range from 50-300 ms. For ELM-free discharges with very high H-factors, the impurity confinement times are much longer than the ELM-free period duration, of order seconds, and are estimates.

V. Impurity Transport in ITB Plasmas

Impurity transport coefficients have also been determined in ITB discharges with argon puffing. ITBs in C-Mod (see Chapter IV on ITBs) are characterized by a strong peaking of the electron density profile inside of the half radius, as demonstrated in Figs.15 and 16. ITBs can be generated by off-axis ICRF heating, which in this case was initiated at 0.7 s, and the density rise can be stabilized with application of on-axis ICRF heating, which in this case was added at 1.25 s. Individual profiles are shown from every 100 ms, starting at 0.575 s. The two chain traces are from the Ohmic L-mode portion of the discharge (at 0.575 and 0.675 s); these profiles are relatively flat. The first dashed curve represents the density profile at 0.775 s, soon after the L-H transition; at this time there was a well defined H-mode edge pedestal, and subsequently the profile filled in toward the center, remaining fairly flat. By 0.875 s the ITB began to develop, apparent in the peaking of the core density and with the barrier foot location near $R = 0.80$ m, $r \sim 10.5$ cm, or $r/a \sim 0.5$. For the next 300 ms, the density profiles (shown as dashed lines) continued to peak in the core, while the outer half of the profile remained quite constant, maintaining the edge pedestal intact, together with the strong ITB, and in the absence of an internal particle source. Without any additional on-axis heating,

the electron density would continue to rise, and impurities would accumulate in the core, eventually destroying the ITB [34]. Between 1.25 and 1.5 s, with 600 kW of additional on-axis ICRF heating, the electron density profile was held constant, as shown by the solid curves.

Besides the arrest of the electron density peaking and the increase in the core ion temperature, there are other beneficial effects from the additional on-axis heating, as is demonstrated in Fig.16. Between 1.35 and 1.5 s, the ambient level of central soft x-ray emission was held constant. Similarly, the additional on-axis heating stemmed the increase of the total radiated power, holding it at a tolerable level of about 50% of the total input power. Likewise, Z_{eff} was maintained at a constant value of 1.8 during this time. In Fig.16 is also shown the ratio of the central electron density to the value at $R = 0.83$ m ($r \sim 13.6$ cm, $r/a \sim 0.65$), well outside of the ITB foot, reiterating the arrest of the density peaking. Impurity transport coefficients for this discharge have been characterized by examining the impurity x-ray brightness profiles from argon which was injected at 0.35 s. Shown in Fig.17 are brightness profiles of argon x-ray lines between 3.94 and 4.00 Å, which originate from helium-like Ar^{16+} and nearby lithium-like satellites [23]. During the Ohmic L-mode phase of this series of similar discharges (as in Fig.15 and 16), the brightness profile was relatively flat (asterisks) while during the steady ITB phase (between 1.25 and 1.5 s), the brightness profile was highly peaked (dots), with over a factor of 20 increase in the core. Similar observations have been made with the (spectrally unresolved) x-ray array [35]. The behavior of the impurity transport coefficients in ITB plasmas near the barrier foot may be addressed from a comparison of these observed argon x-ray brightness profiles with those predicted using MIST, in conjunction with the atomic physics package LINES [26]. Shown in Fig.17 by the chain curve is the calculated brightness profile using the previously determined L-mode transport coefficient profiles, which are reproduced in Fig.18, also by the chain curves. In Ohmic L-mode the impurity diffusion coefficient is highly anomalous while there is no evidence for any inward convection velocity. During the steady ITB phase, a radical modification to the impurity transport coefficients

is necessary in order to reproduce the highly peaked argon x-ray brightness profile. Simply using the ITB electron density and temperature profiles, together with the argon density profiles calculated using the L-mode impurity transport coefficients, leads to the upperchain curve of Fig.17, which has the same shape as the L-mode brightness profile and does not represent the observed profile. The solid curve of Fig.17, which does an excellent job of matching the data, was generated using the transport coefficients shown as solid lines in Fig.18. These are very close to the calculated neo-classical impurity transport coefficient profiles shown by the dashed curves. For these ITB plasmas both the thermal and impurity transport approaches neo-classical levels in the core. The impurity transport is characterized by greatly reduced diffusion and a strong inward convection velocity in the vicinity of the large ion (and electron) density gradient. It should be noted that using only steady state impurity brightness profiles does not uniquely determine the impurity transport coefficients; modeling of temporally evolving brightness profiles following impurity injection is necessary. Other combinations of diffusion and convection profiles can also match the observed argon x-ray brightness profiles during the ITB phase. However, no match could be found using a combination of the neo-classical convection velocity and the anomalous diffusion coefficient. Regardless of the actual impurity diffusion coefficient and convection velocity profiles, the deduced impurity density profiles (and x-ray brightness profiles) are highly peaked near the plasma core, more so than the electron density profile. This analysis could not be performed for ITB plasmas with only on-axis heating since the electron and impurity density profiles are not steady state. The observations are consistent with the impurity transport approaching neo-classical levels in ITB plasmas.

VI. Parallel Impurity Transport

The previous sections addressed the issue of perpendicular impurity transport, which has anomalously high diffusion in L-mode plasmas, and with transport coefficients whose values approach neo-classical levels in H-mode regimes that have

reduced turbulence levels. In this section parallel impurity will be explored. Near the plasma edge, neo-classical parallel impurity transport manifests itself in an up-down asymmetry of impurity densities. Shown in Fig.19 are x-ray spectra of Ar^{16+} [36] taken from two chords tangent to the same flux surface (from EFIT [37]) which crosses the plasma midplane at a major radius of 0.812 m ($r/a \sim 0.6$) for an L-mode discharge with the ion $\mathbf{B} \times \nabla \mathbf{B}$ drift downward. The plasma center, denoted in the figure by the '+' sign, was located at $R = 0.681$ m and $Z = -0.7$ cm, so these spectra are from flux surfaces characterized by $r = 13.1$ cm (the difference between 81.2 cm and 68.1 cm). The vacuum vessel center is shown by the 'x'. The individual lines of sight are depicted in the inset in the figure, and the spectrum shown by the solid curve was from a view which crossed the vertical plane of $R = 0.67$ m at $Z = +16.5$ cm (solid line), and the dotted spectrum was from $Z = -18.0$ cm (dotted line). The two spectra are nearly identical in intensity, indicating that the argon x-ray emission on this flux surface is constant. (The mappings of the two lines of sight back to the plasma midplane are shown by the dot and asterisk.) These spectra are quite different from the central chord spectrum, in that the overall intensity is greatly reduced, and all line intensities have grown relative to the resonance line. The lines are narrow due to the lower ion temperature at this radius. Also shown in the figure by the thin line is a synthetic spectrum for these viewing chords, again in good agreement with the observed spectra. Spectra obtained from near the last closed flux surface for a similar discharge are presented in Fig.20. Shown by the solid curve is a spectrum from along the solid sightline viewing the top of the plasma, characterized by $R = 0.894$ m, $r = 21.1$ cm and $Z = +28.9$ cm. This spectrum is dominated by the forbidden line z, as the resonance line has fallen in intensity compared to Fig.19, the satellites have all disappeared, and the lines are all very narrow. This is indicative of a recombining plasma [23], where the line population is overwhelmingly dominated by radiative recombination of hydrogen-like Ar^{17+} . The reason that Ar^{17+} exists at this radius, where the electron temperature is ~ 200 eV, is because of the fast radial (outward) impurity transport in L-mode, characterized by $D = 0.5$ m²/s. Shown by the dotted curve is

a spectrum from along the dotted sightline viewing the bottom of the plasma but near the same flux surface, at $R = 0.885$ m, $r = 20.2$ cm and $Z = -30.9$ cm. The brightness of this spectrum is about a factor of 6 lower than the spectrum taken from the top of the plasma. Also shown in the figure by the thin line is a synthetic spectrum for these viewing chords, normalized to the top spectrum, again in good agreement with the observed spectra. The plasmas of Figs.19 and 20 had the ion $\mathbf{B} \times \nabla \mathbf{B}$ drift direction toward the bottom of the machine (plasma current and toroidal field in the clockwise direction from above), and the single null X-point was at the bottom as well. Alcator C-Mod has also been operated with the ion $\mathbf{B} \times \nabla \mathbf{B}$ drift direction toward the top of the machine, by reversing the toroidal magnetic field direction (the plasma current direction was simultaneously reversed). Argon x-ray spectra have been obtained for plasmas with similar discharge conditions as in Figs.19 and 20. Shown in Fig.21 by the solid curve is a spectrum from the solid sightline characterized by $R = 0.874$ m, $r = 19.5$ cm and $Z = +25.9$ cm, and by the dotted curve from $R = 0.872$ m, $r = 19.3$ cm and $Z = -28.9$ cm. In this case, with the ion $\mathbf{B} \times \nabla \mathbf{B}$ drift direction upward, the spectrum from the bottom of the plasma was about a factor of 8 brighter. (The X-point was located in the bottom of the machine for these spectra.) Figs.20 and 21 demonstrate that impurity x-ray emission is not constant on flux surfaces near the edge, and that this large up-down impurity asymmetry is in the direction opposite to that of the ion $\mathbf{B} \times \nabla \mathbf{B}$ drift direction. These results are summarized in Fig.22, where the brightness of the forbidden line is plotted as a function of the vertical distance from the sightline to the vacuum vessel center at $R = 0.67$ m. The asterisks were obtained during the low density plateau of a sequence of identical L-mode discharges, with the ion $\mathbf{B} \times \nabla \mathbf{B}$ drift direction down. The asymmetry begins at the top of the plasma around +20 cm, and extends out to the last closed flux surface, with a maximum brightness ratio (of the top to the bottom) of about a factor of 10. The points shown as boxes were obtained from a series of discharges with similar conditions, except with the ion $\mathbf{B} \times \nabla \mathbf{B}$ drift direction up, and in this case the asymmetry (enhancement) was at the bottom of the plasma. Modeling of the observed up-down impurity densities

is in reasonable agreement [36], both in magnitude and direction, with neo-classical predictions [38,39]. For the plasmas of Figs.20 and 21, the electron density and temperature profiles with up-down symmetric at $r/a = 0.9$. In both cases the X-point was down so up-down neutral density asymmetries should have been the same.

VII. Discussion and Conclusions

Perpendicular impurity transport coefficients have been determined using laser blow-off injection of Sc and CaF₂ and measured emissivity profiles, in conjunction with the impurity transport code MIST and the atomic physics package LINEST. L-mode impurity confinement is short ($\tau \sim 20$ ms) with a diffusivity $D \sim 0.5$ m²/s over most of the plasma, anomalously large compared to neo-classical values. In EDA H-mode plasmas impurity confinement times are considerably longer, in the range of 50-200 ms, with D greatly reduced in the edge pedestal region, and with substantial inward convection, also at the plasma edge. In ELM-free H-mode discharges, the impurity confinement is very long, and the edge transport coefficients approach the neo-classical levels. For ITB plasmas, there is strong impurity accumulation inside of the barrier foot.

Steady state impurity densities near the plasma edge are not constant on flux surfaces, with large (a factor of ~ 10) up-down asymmetries. The impurity density is enhanced opposite to the ion $\mathbf{B} \times \nabla \mathbf{B}$ drift direction, and is consistent with modeling of neo-classical parallel impurity transport.

VIII. Acknowledgements

The authors thank C. Fiore for ion temperature measurements and the Alcator C-Mod operations and ICRF groups for expert running of the tokamak. Work supported at MIT by DoE Contract No. DE-FC02-99ER54512.

References

- [1] J. Wesson, Tokamaks, Oxford University Press, Oxford (1987).
- [2] M. Shimada, Fusion Engineering and Design **15** (1992) 325.
- [3] J.E.Rice, E.S.Marmor, B.Lipschultz and J.L.Terry, Nucl. Fusion **24** (1984) 329.
- [4] E. Marmor, J. Cecchi and S. Cohen, Rev. Sci. Instrum. **46** (1975) 1149.
- [5] E. S. Marmor, J. E. Rice and S. L. Allen, Phys Rev. Lett. **45** (1980) 2025.
- [6] TFR Group, Phys. Lett. **87A** (1982) 169.
- [7] E. S. Marmor, J. E. Rice, J. L. Terry and F. Seguin, Nucl. Fusion **22** (1982) 1567.
- [8] TFR Group, Nucl. Fusion **23** (1983) 559.
- [9] B.C. Stratton, A.T. Ramsey, F.P. Boody, C.E. Bush, R.J. Fonck, R.J. Groebner, R.A. Hulse, R.K. Richards and J. Schivell, Nucl. Fusion **27** (1987) 1147.
- [10] G. Fussman, J. Hofmann, G. Janeschitz and K. Krieger, J. Nucl. Mater. **162** (1989) 14.
- [11] K. Ida, R.J. Fonck, S. Sesnic, R.A. Hulse, B. LeBlanc and S.F. Paul, Nucl. Fusion **29** (1989) 231.
- [12] M.E. Perry, N.H. Brooks, D.A. Content, R.A. Hulse, M.A. Mahdavi and H.W. Moos, Nucl. Fusion **31** (1991) 1859.
- [13] D. Pasini, R.Giannella, L.L.Taroni, M.Mattioli, B.Denne-Hinnov, N.Hawkes, G.Magyar and H.Weisen, Plasma Physics and Controlled Fusion **34** (1992) 677.
- [14] J.E.Rice et al., Phys. Plasmas **4** (1997) 1605.
- [15] J.E.Rice et al., Phys. Plasmas **7** (2000) 1825.
- [16] T.Sunn Pedersen et al., Nucl. Fusion **40** (2000) 1795.
- [17] H. Takenaga et al., Phys. Plasmas **8** (2001) 2217.
- [18] J.E.Rice et al., Nucl. Fusion **42** (2002) 510.
- [19] R. Dux et al., Nucl. Fusion **44** (2004) 260.
- [20] J.E.Rice and E.S.Marmor, Rev. Sci. Instrum. **61** (1990) 2753.
- [21] J.E.Rice et al., J. Phys. B **28** (1995) 893
- [22] L. A. Vainshtein and U. I. Safronova, Phys. Scr. **31** (1985) 519.

- [23] J.E.Rice et al., Phys. Rev. A **35** (1987) 3033.
- [24] M.A. Graf, J.E. Rice, J.L. Terry, E.S. Marmor, J.A. Goetz, G.M. McCracken, F. Bombarda and M.J. May, Rev. Sci. Instrum. **66** (1995) 636.
- [25] R. A. Hulse, Nucl. Tech./Fus. **3** (1983) 259.
- [26] M.A.Graf, 'Impurity Injection Experiments on the Alcator C-Mod Tokamak', Ph.D. Dissertation, Massachusetts Institute of Technology (1995)
- [27] R.Mewe, Astron. and Astrophys. **20** (1972) 215.
- [28] R. Mewe and J. Schrijver, Astron. Astrophys. **65**, (1978) 99.
- [29] R. Mewe, J. Schrijver and J. Sylwester, Astron. Astrophys. **87** (1980) 55
- [30] F. Bely-DuBau, J. DuBau, P. Faucher *et al.*, Mon. Not. R. Astr. Soc. **201** (1982) 1155.
- [31] L.A. Vainshtein and U.I. Safronova, Atomic Data and Nuclear Data Tables **21** (1978) 49.
- [32] W.L. Acton, J.L. Culhane, A.H. Gabriel *et al.*, Astrophys. J. **244** (1980) L137.
- [33] R. Hawryluk, S. Suckewer and S. Hirshman, Nucl. Fusion **19** (1979) 607.
- [34] W.A.Houlberg et al., Phys. Plasmas **4** (1997) 3230.
- [35] J.E.Rice et al., Nucl. Fusion **41** (2001) 277.
- [36] J.E.Rice et al., Nucl. Fusion **37** (1997) 241.
- [37] L. L. Lao, H. St.John, R.D. Stambaugh, A.G. Kellman and W. Pfeiffer, Nucl. Fusion **25** (1985) 1611.
- [38] K.H.Burrell and S.K.Wong, Nucl. Fusion **19** (1979) 1571.
- [39] C.T.Hsu and D.J.Sigmar, Plasma Phys. Control. Fusion **32** (1990) 499.

Figure Captions

Fig. 1 The time histories, from top to bottom, of the plasma current, central electron density and temperature, Sc^{19+} x-ray emission and Z_{eff} for an L-mode discharge with scandium injection at 0.57 s.

Fig. 2 The observed brightness time histories for lithium-like (asterisks) and helium-like (dots) line emission for a scandium injection at 0.75 s into an L-mode plasma, and the simulations (curves). The x-ray data and simulation have been increased by a factor of 100 for direct comparison with the VUV traces. (1 GR = 10^{15} photons/cm²/sec.)

Fig. 3 The electron density and temperature profiles (top) and the impurity diffusion coefficient profile (bottom) for L-mode.

Fig. 4 Observed time histories of helium-like Sc^{19+} emission along chords tangent to r/a of 0.10 (top), 0.39 (middle) and 0.69 (bottom), with code predictions (smooth lines).

Fig. 5 Parameter time histories for an EDA H-mode plasma with a trace CaF_2 injection at 0.8 s. From top to bottom, the plasma stored energy, the central density (electron-solid line, calcium-chain line, $\times 10^5$), the central temperature (electron-with sawteeth, ion-smooth), the ICRF input power, the D_α brightness and the central chord x-ray brightness ($3.17 \text{ \AA} < \lambda < 3.22 \text{ \AA}$).

Fig. 6 A surface plot of the x-ray brightness between 3.17 and 3.22 \AA , as a function of time.

Fig. 7 The normalized brightness time histories of Ca^{18+} , 3.1773 \AA (dots), total x-ray signal between 3.17 and 3.22 \AA (solid thick line), Ca^{17+} , 344.8 \AA (chain line) and Ca^{16+} , 192.9 \AA (dashed line) are shown in the top frame. Also shown by the

thin smooth line is an exponential fit to the x-ray signal, with a decay time of 68 ms. In the bottom frame are the corresponding simulated time histories.

Fig. 8 The edge electron density (chain) and temperature (solid) profiles are shown in the top frame. The impurity diffusion coefficient profile (top frame) and convection velocity profile (bottom frame) used in the simulation are shown by the solid lines, while the calculated neo-classical profiles are shown by the chain curves. The LCFS was at 22.1 cm.

Fig. 9 Measured x-ray (resonance line of Ca^{18+} , 3.1773 Å, at 0.87 s, top frame) and VUV (resonance line of Ca^{16+} , 192.9 Å, at 0.815 s, bottom frame) brightness profiles are depicted as the dots, and the simulations are shown by the solid curves.

Fig. 10 Contour plot of the measured Ca^{18+} resonance line brightness (thick lines) and simulation (smooth thin lines). Each contour is 0.01 GR.

Fig. 11 Contour plot of the measured Ca^{16+} resonance line brightness (thick lines) and simulation (smooth thin lines). Each contour is 1 GR.

Fig. 12 The soft x-ray emissivity profile as a function of radius near the LCFS (22.1 cm) shown (bottom frame) as the points, with the simulation shown by the thick line. The edge electron density and temperature profiles are shown in the top frame.

Fig. 13 Parameter time histories for an ELM-free H-mode plasma. From top to bottom are shown the Sc^{18+} signal, the D_α brightness, the total radiated power and electron density, the plasma stored energy and the input ICRF power.

Fig. 14 The measured impurity confinement times as a function of ITER 89-P H-factor.

Fig. 15 Electron density profiles shown every 100 ms, beginning at 0.575 s, for an ITB plasma. The chain curves are from the Ohmic L-mode portion of the discharge, while the dashed and solid traces are from the evolving and steady state ITB phases, respectively. The L-H transition time was 0.76 s and the ITB began forming at 0.88 s.

Fig. 16 Time histories of the central soft x-ray brightness (top), total radiated power (2nd frame) and Z_{eff} (3rd frame) for an ITB discharge. In the bottom frame is ratio of the central electron density and that at $R = 0.83$ m ($r/a = 0.7$), outside of the ITB foot. The L-H transition time was 0.76 s and the ITB began forming at 0.88 s.

Fig. 17 Measured x-ray brightness profiles (3.94 - 4.00 Å, from helium-like Ar^{16+} and Li-like satellites) from the Ohmic L-mode phase (asterisks) and steady state ITB phase (dots). MIST simulations are shown by the lines; dash-dot curves using the L-mode transport coefficients, solid curve with the ITB transport coefficients. The dashed line represents the total argon density profile during the steady ITB phase.

Fig. 18 Radial profiles of the impurity diffusion coefficients (top frame) and convection velocities (bottom frame) used in the MIST simulations. Ohmic L-mode (chain), steady state ITB (solid) and neo-classical values for the ITB plasma (dashed).

Fig. 19 Spectra from a top viewing chord (solid) and a bottom viewing chord (dotted) from $r/a \sim .6$. A synthetic spectrum is shown by the thin line. The chordal views are shown in the inset.

Fig. 20 Spectra from a top viewing chord (solid) and a bottom viewing chord (dotted) from $r/a \sim .9$. In this case, the ion $\mathbf{B} \times \nabla \mathbf{B}$ drift was downward. A synthetic spectrum is shown by the thin line, normalized to the top spectrum.

Fig. 21 Spectra from a top viewing chord (solid) and a bottom viewing chord (dotted) from $r/a \sim .9$. In this case, the ion $\mathbf{B} \times \nabla \mathbf{B}$ drift was upward.

Fig. 22 Vertical brightness profiles for the forbidden line with the ion $\mathbf{B} \times \nabla \mathbf{B}$ drift downward (asterisks) and upward (boxes).

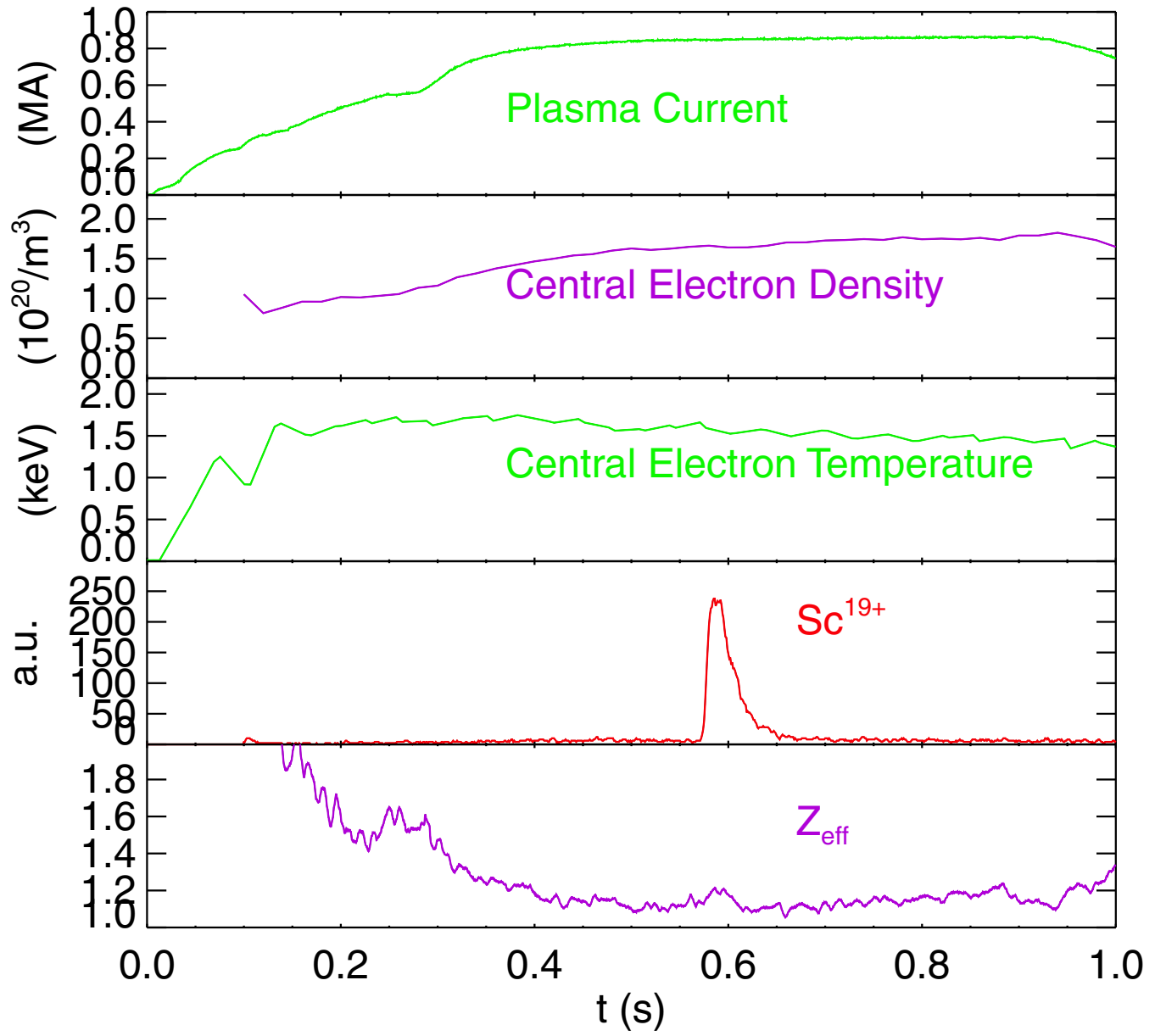


Figure 1

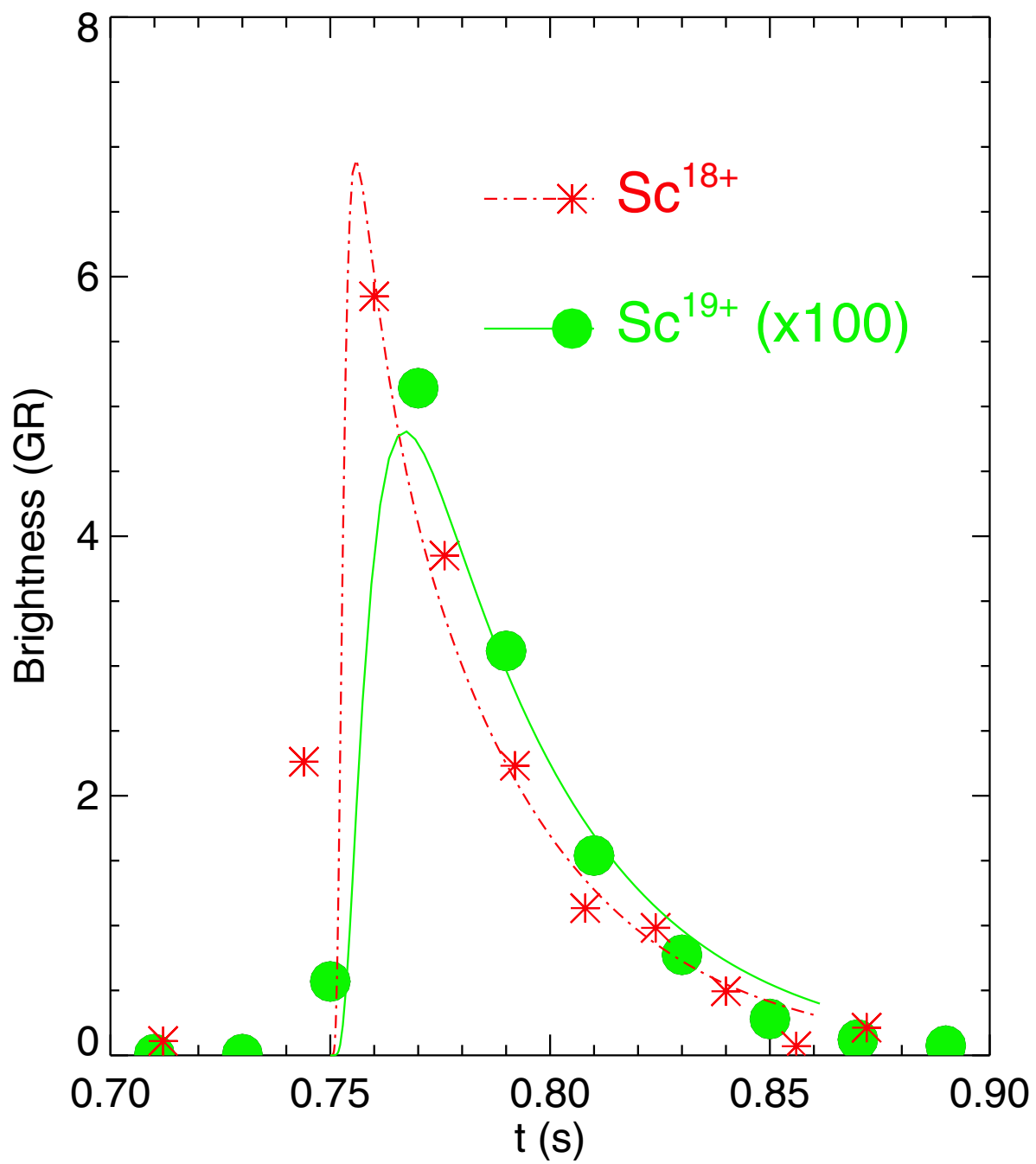


Figure 2

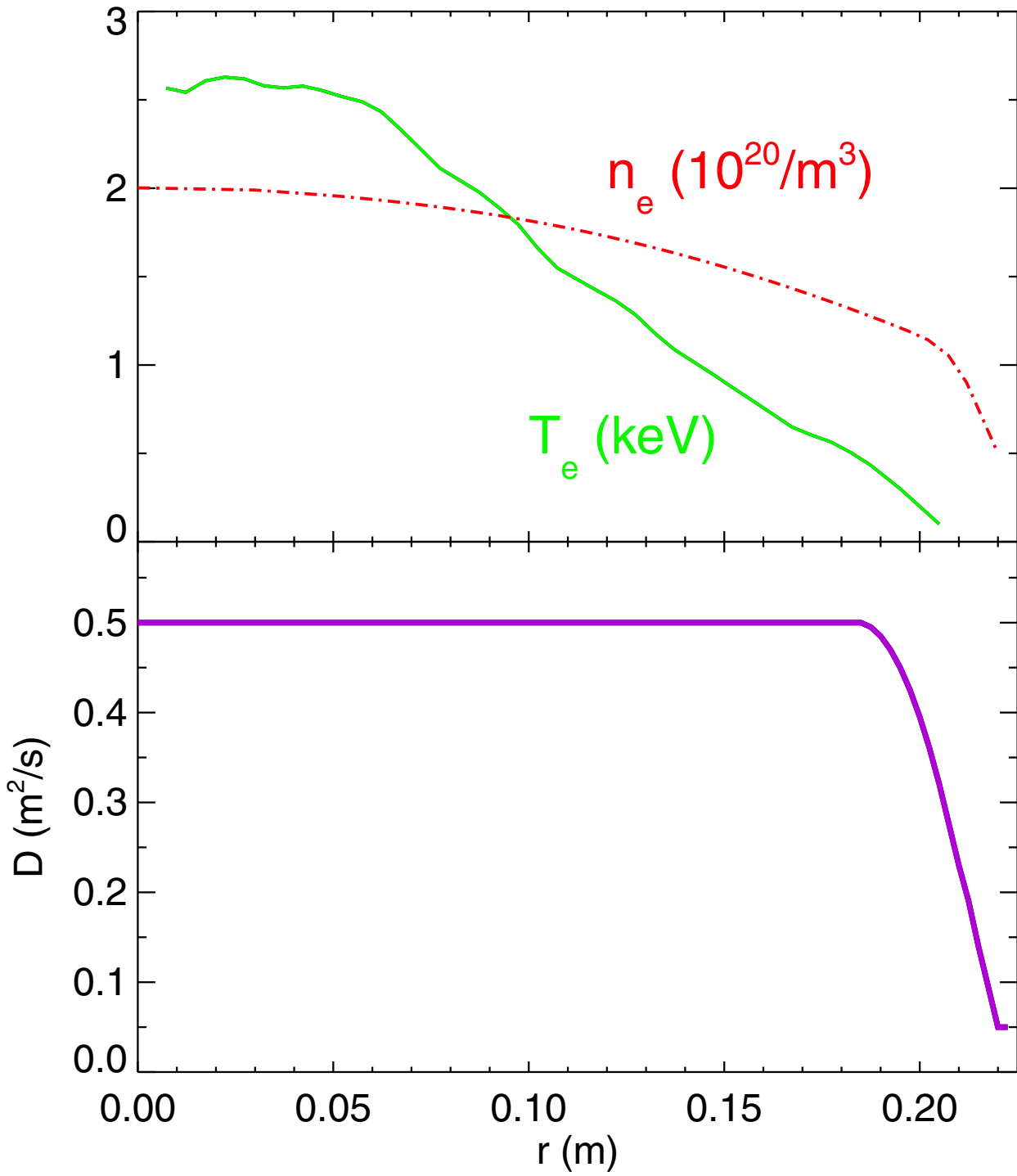


Figure 3

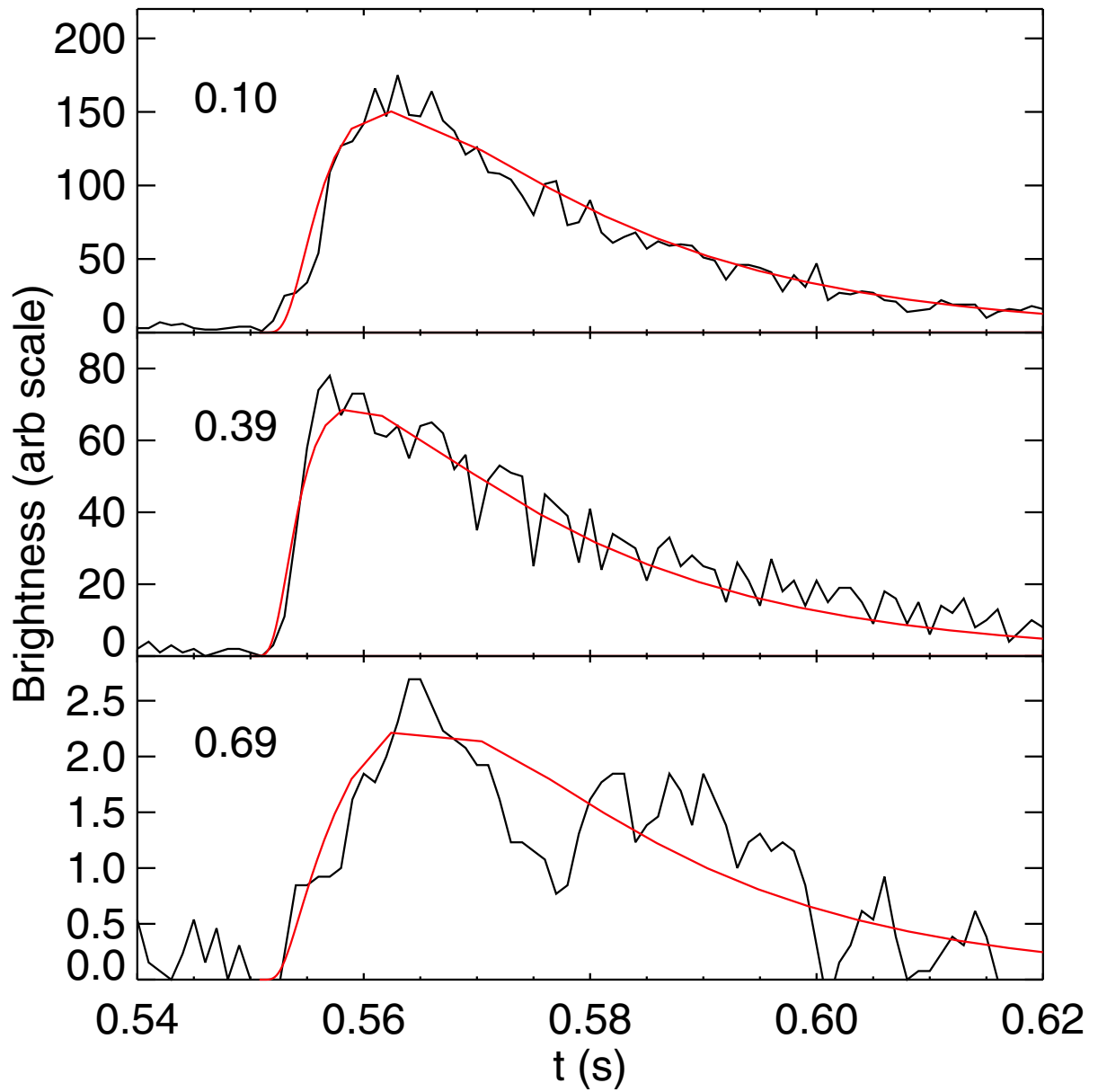


Figure 4

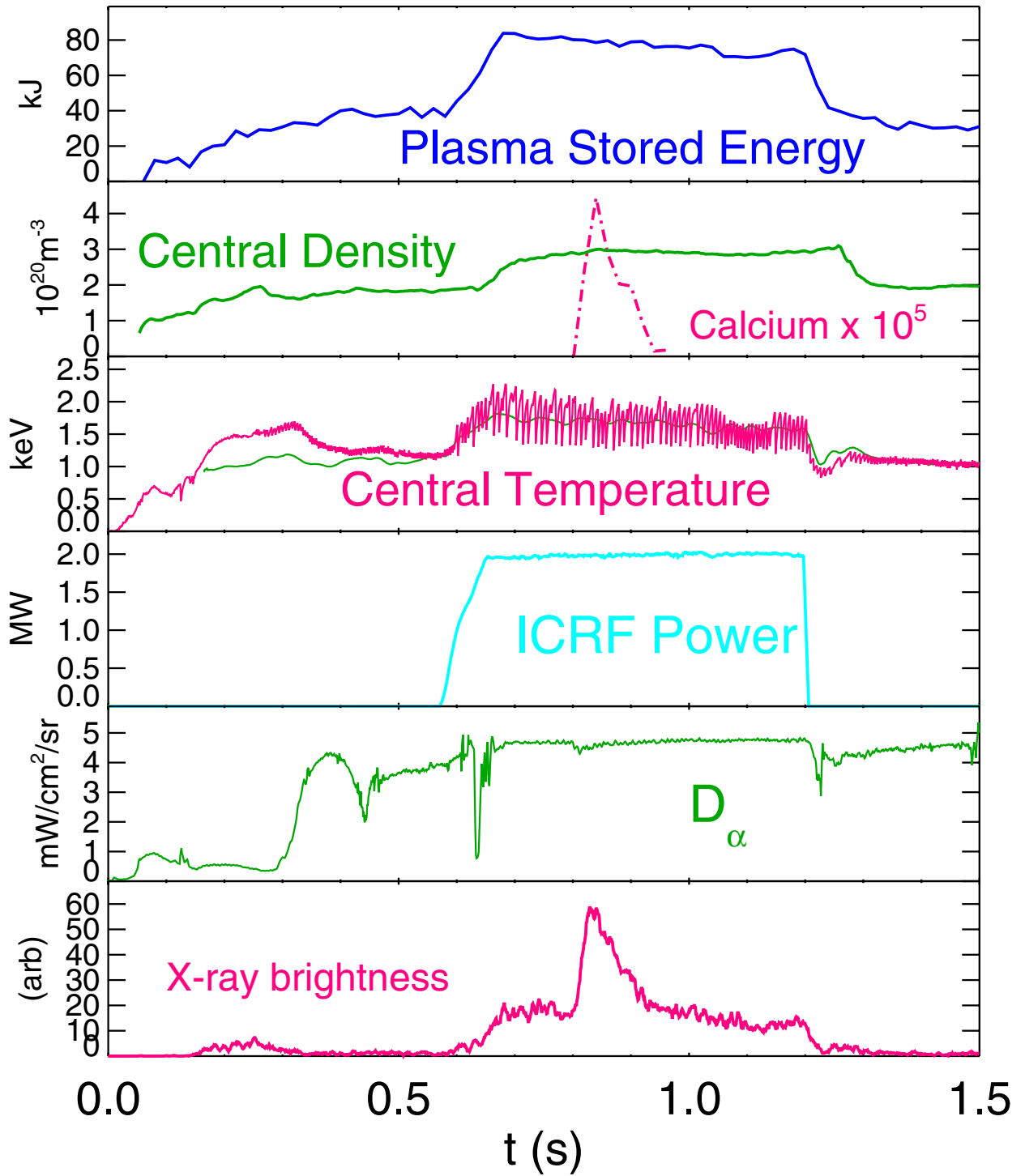


Figure 5
26

Ca¹⁸⁺

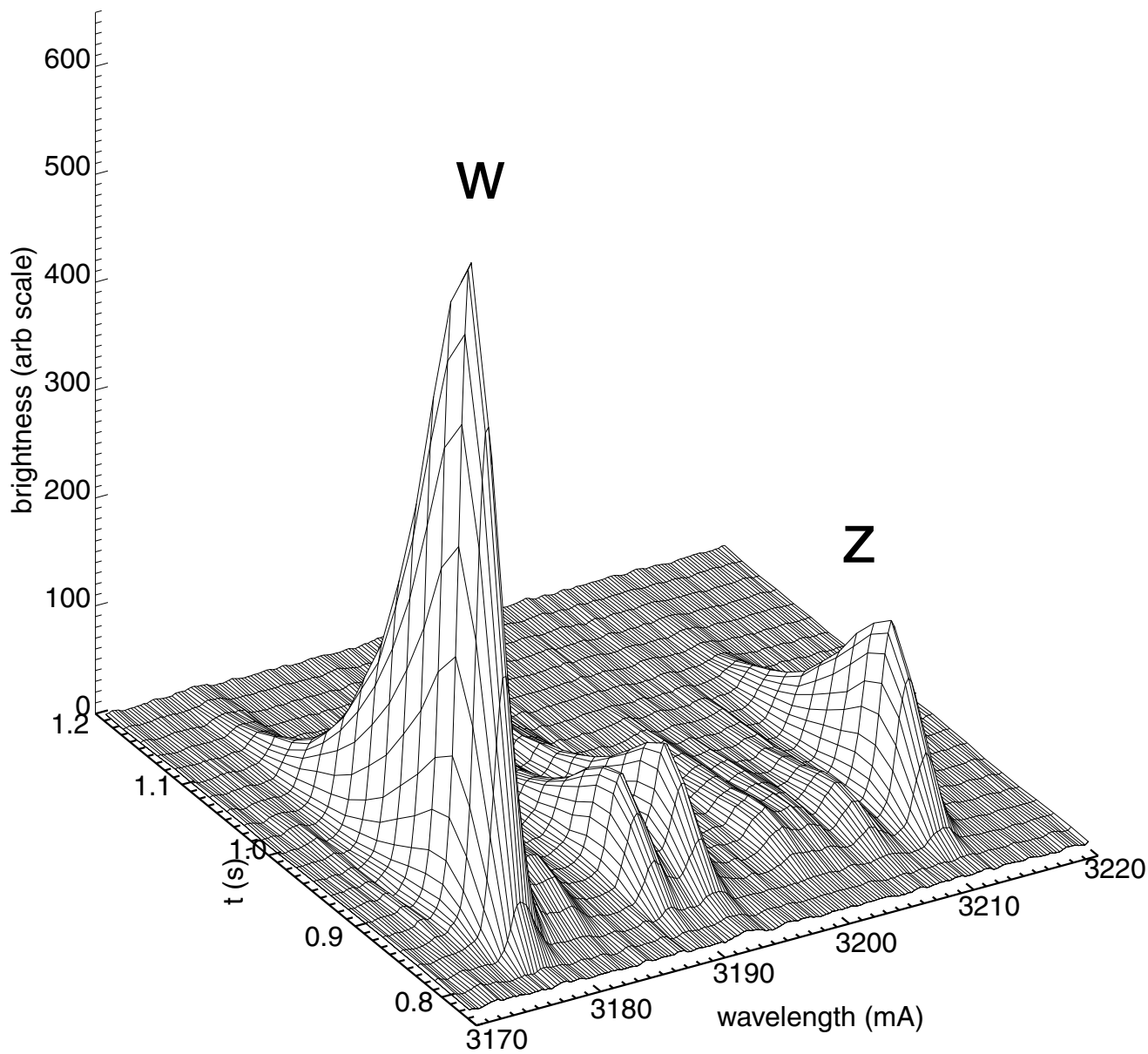


Figure 6

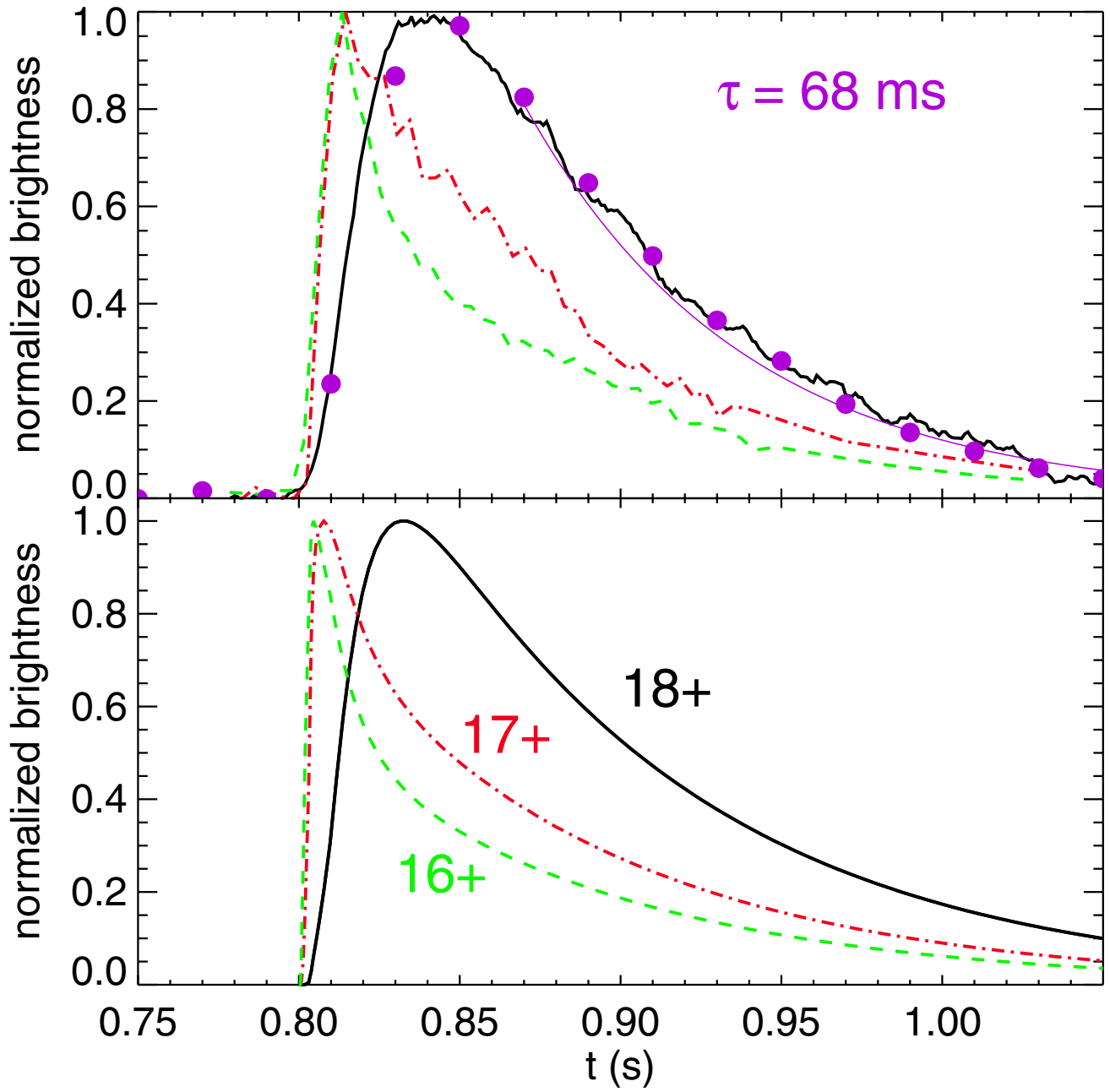


Figure 7

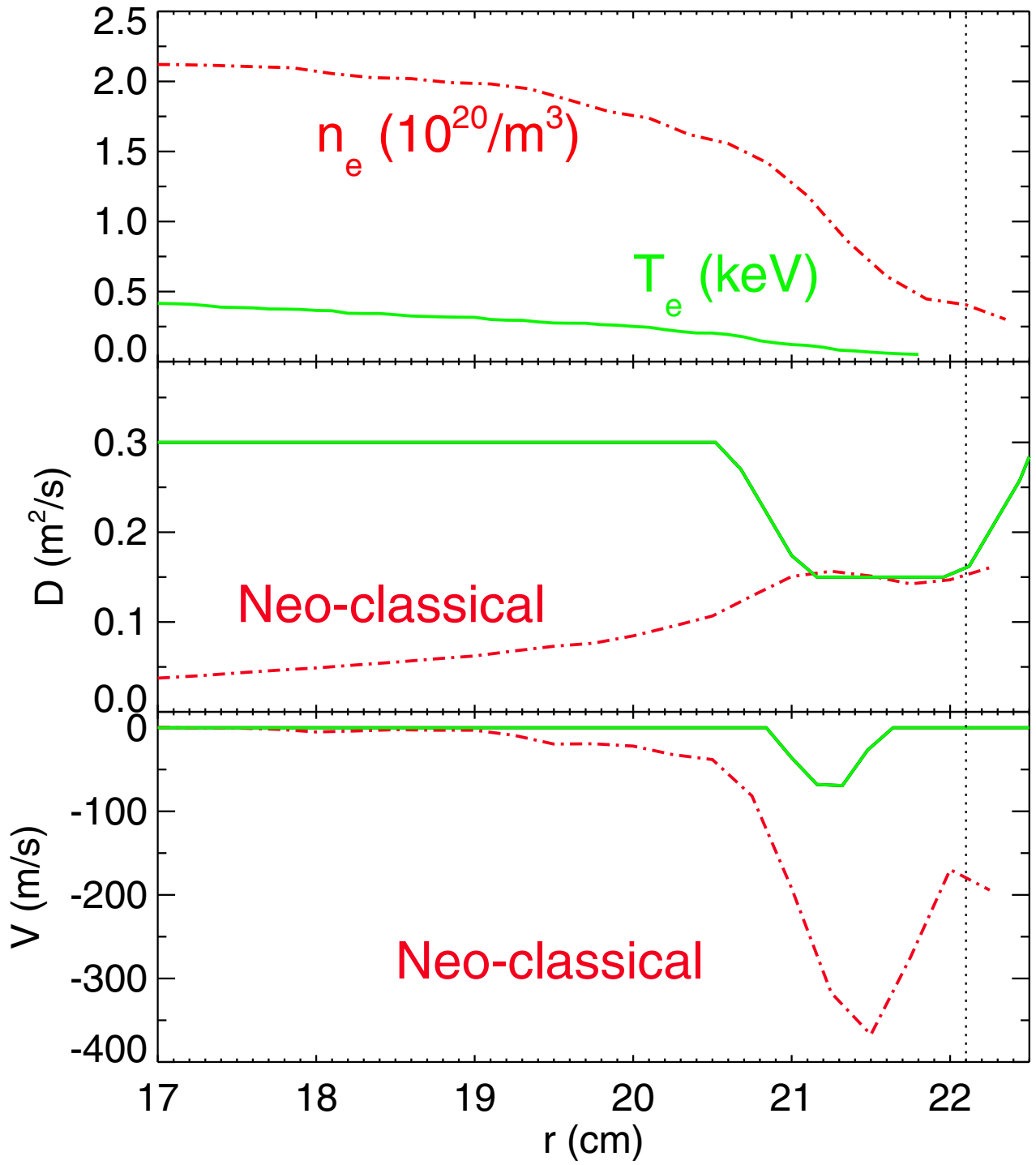


Figure 8

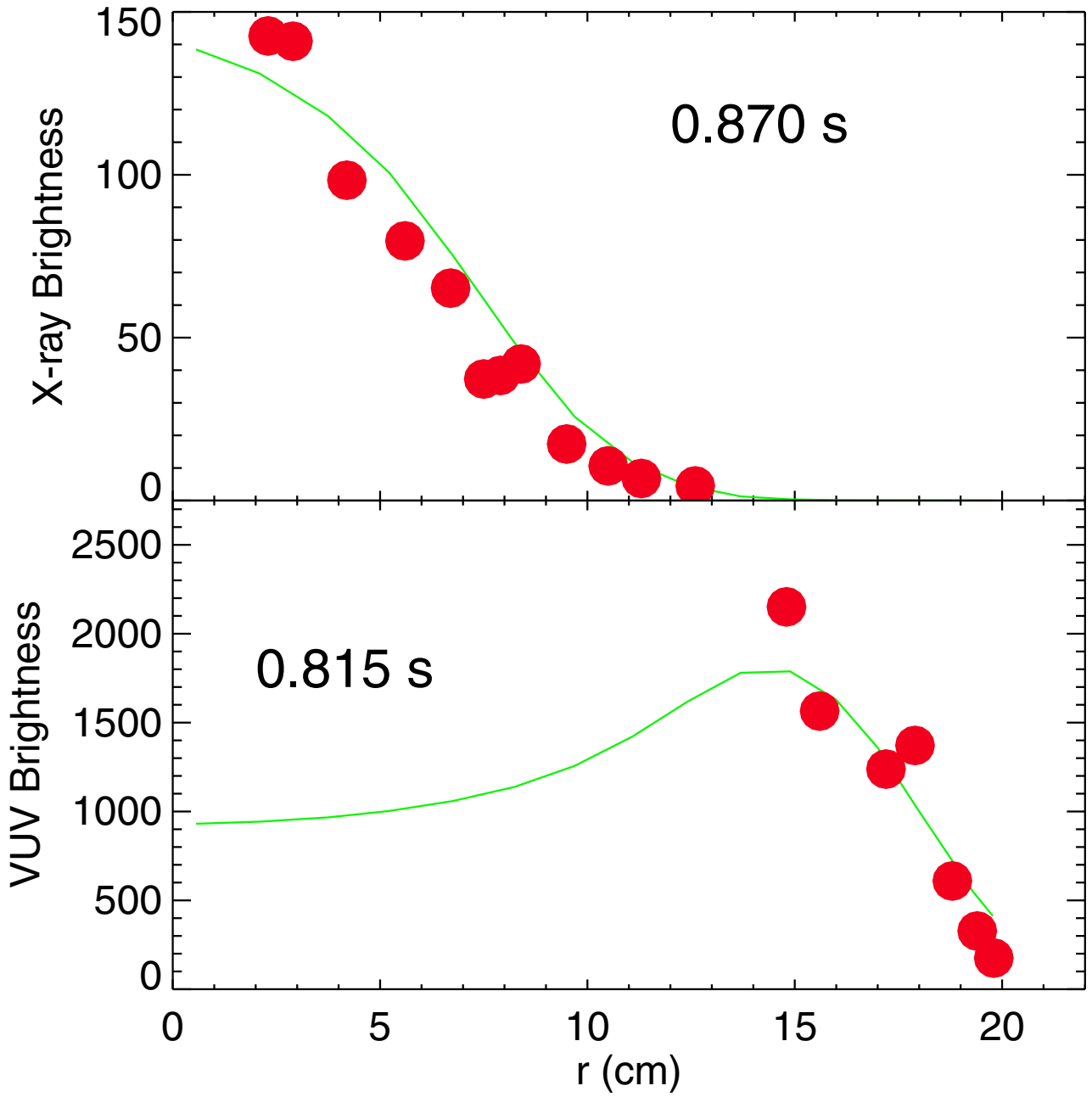


Figure 9

Ca¹⁸⁺ w Brightness Contours

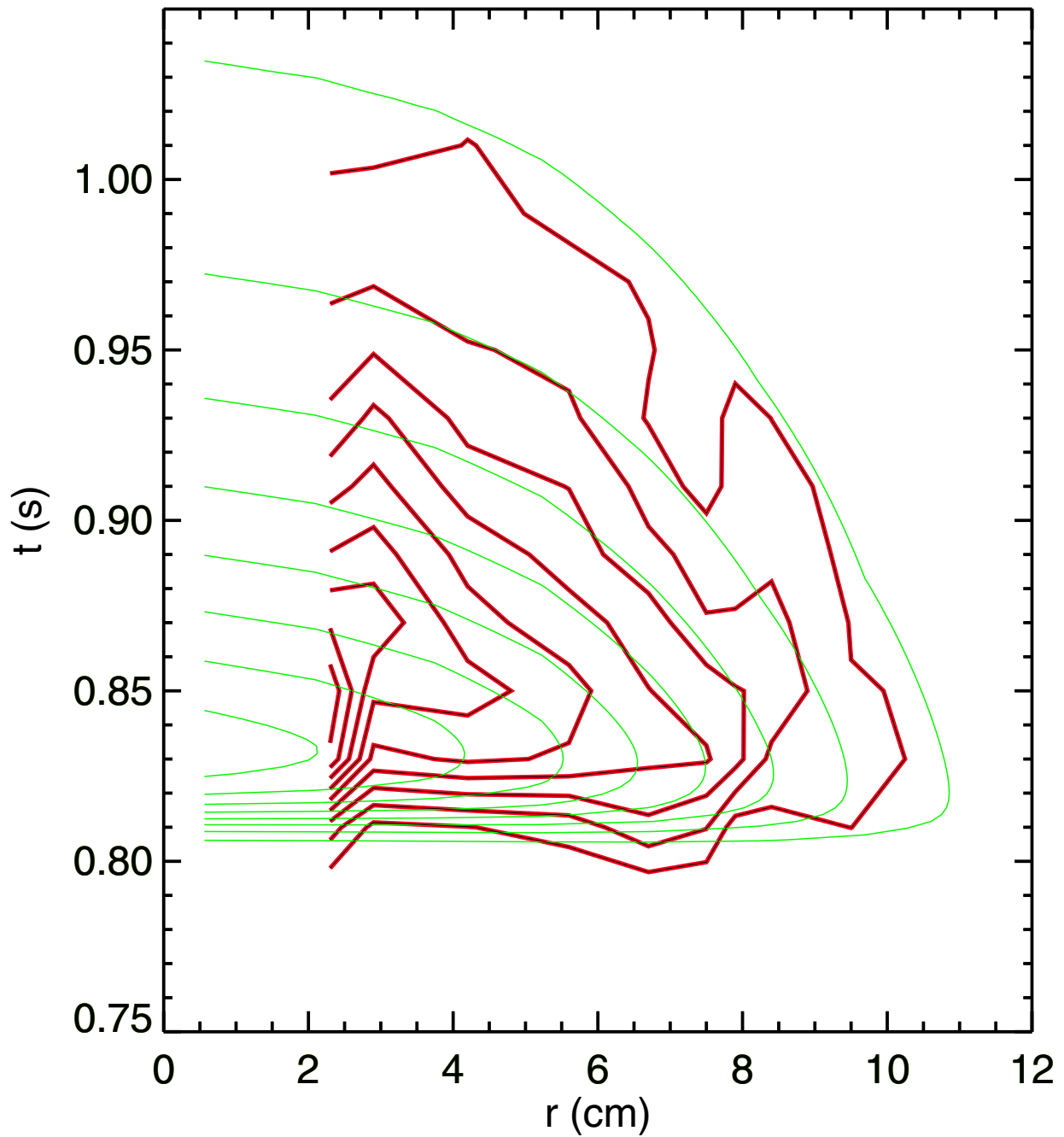


Figure 10

Ca¹⁶⁺ 192Å Brightness Contours

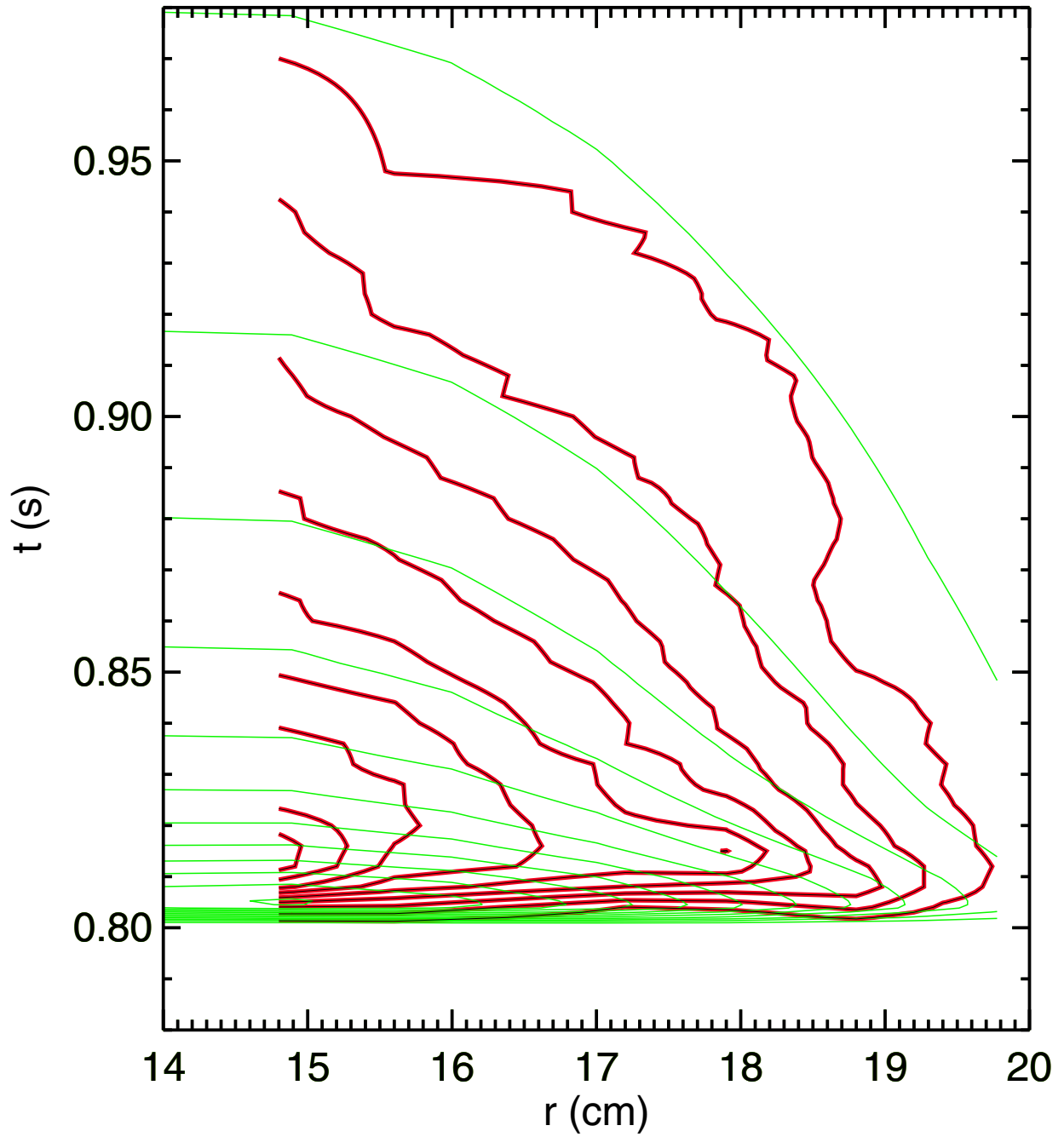


Figure 11

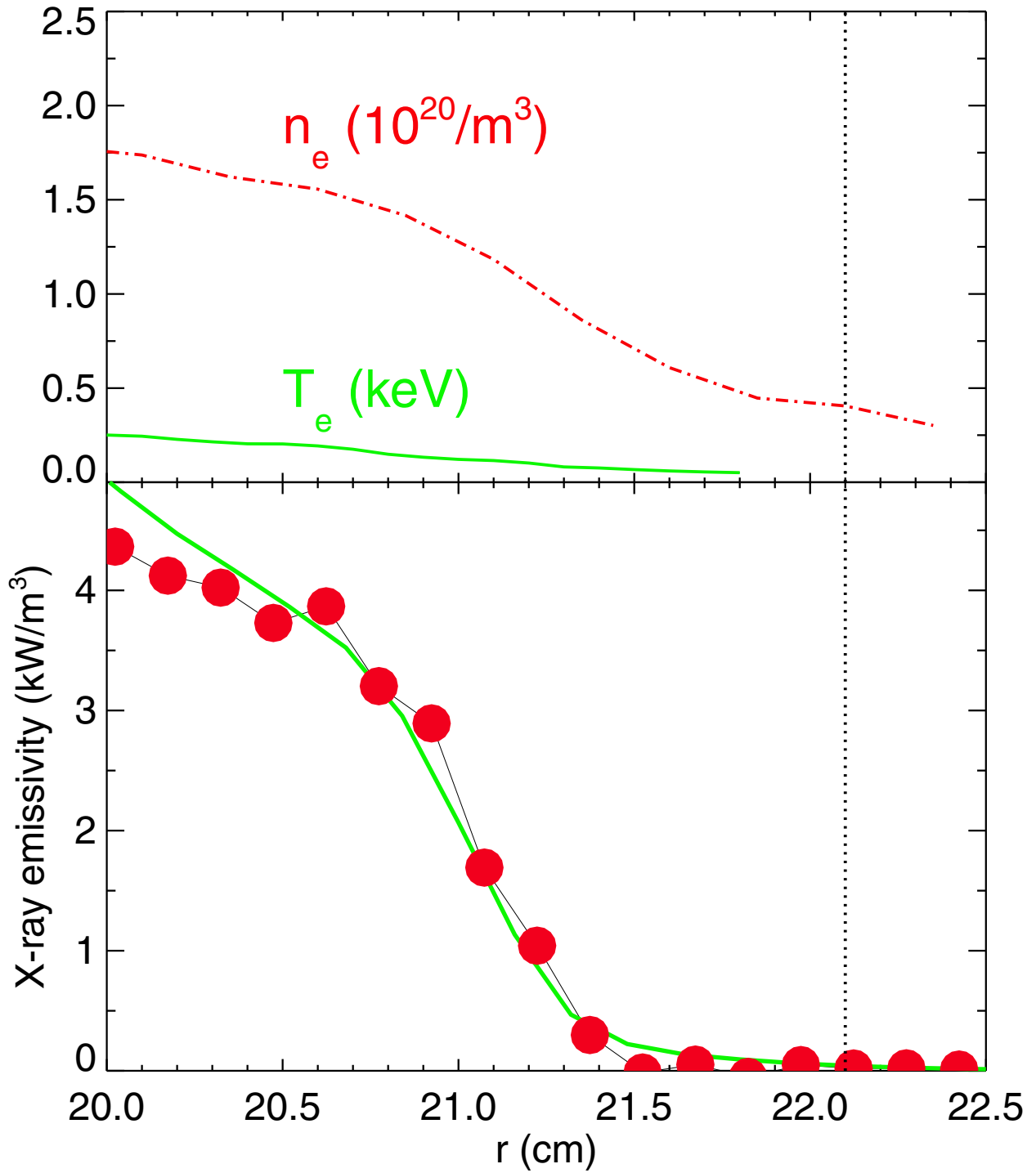


Figure 12

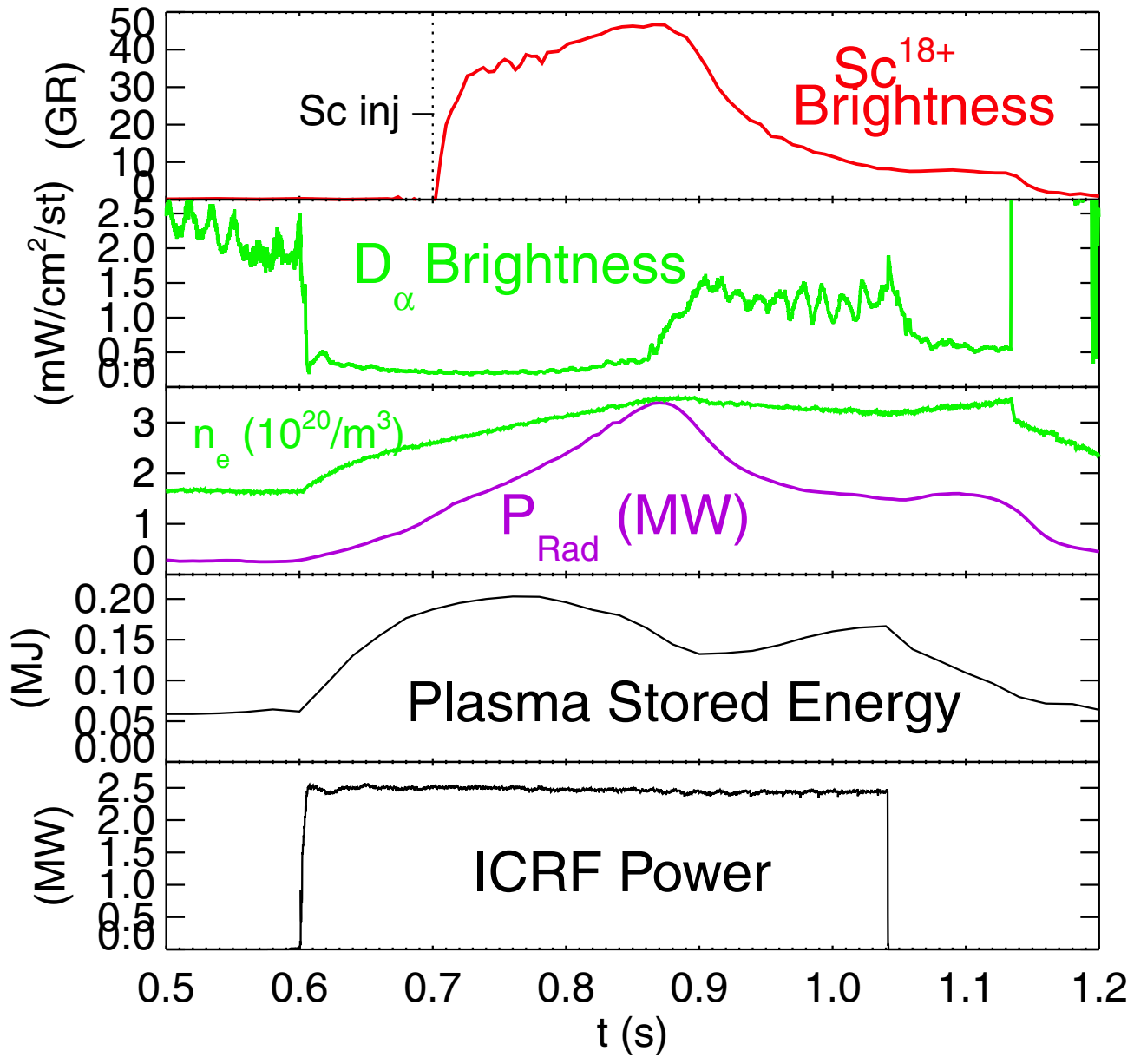


Figure 13

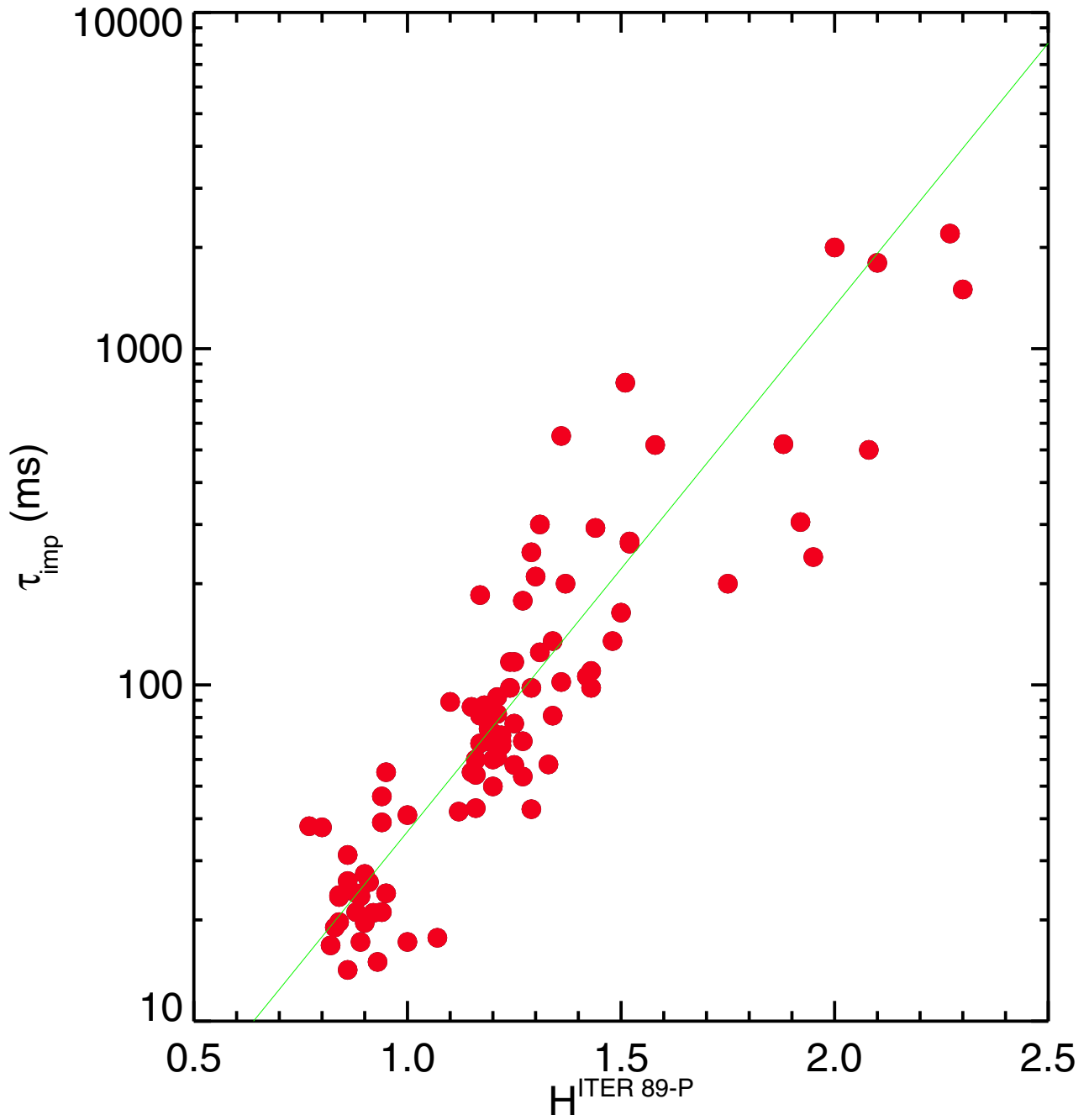


Figure 14

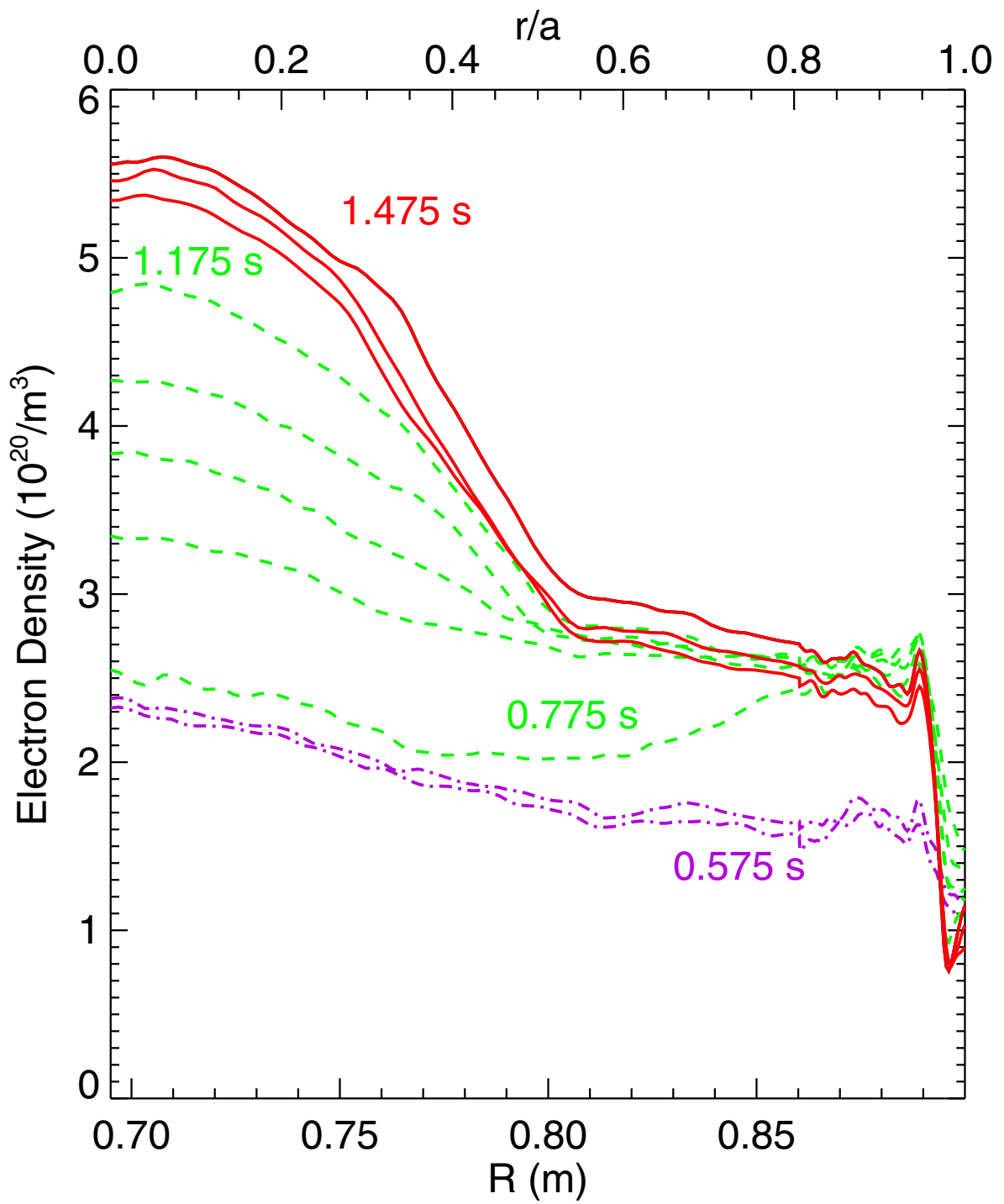


Figure 15

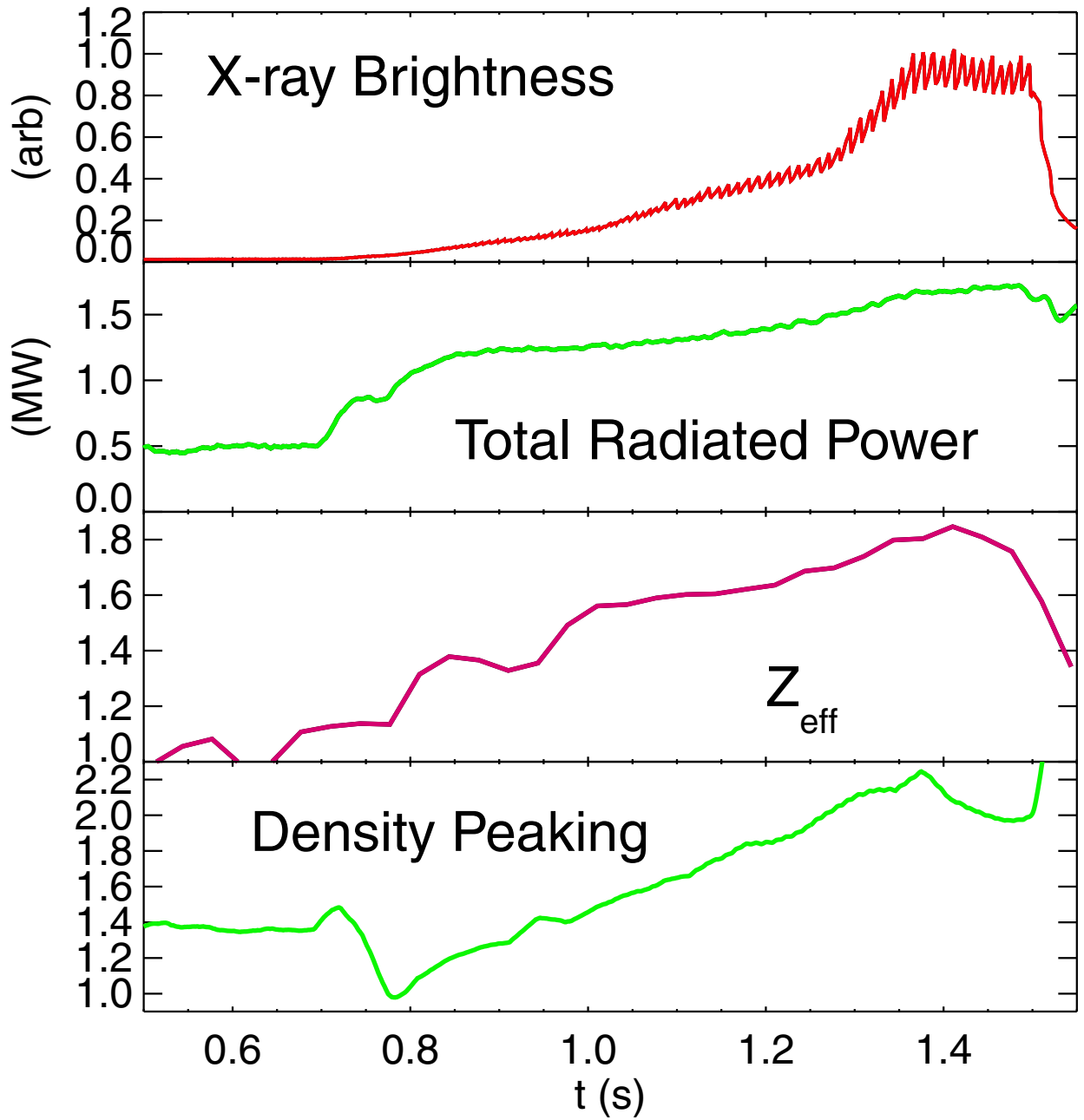


Figure 16

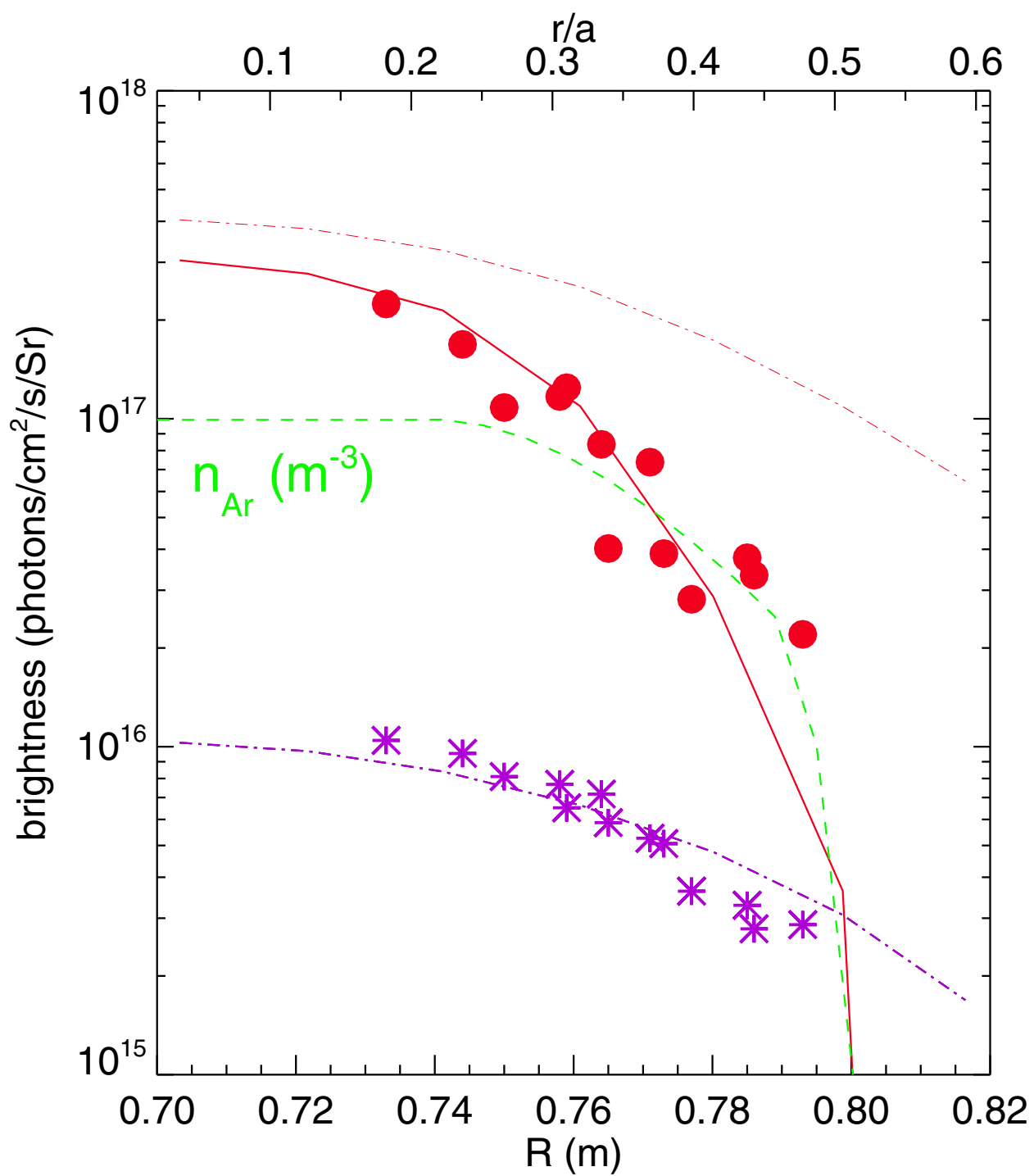


Figure 17

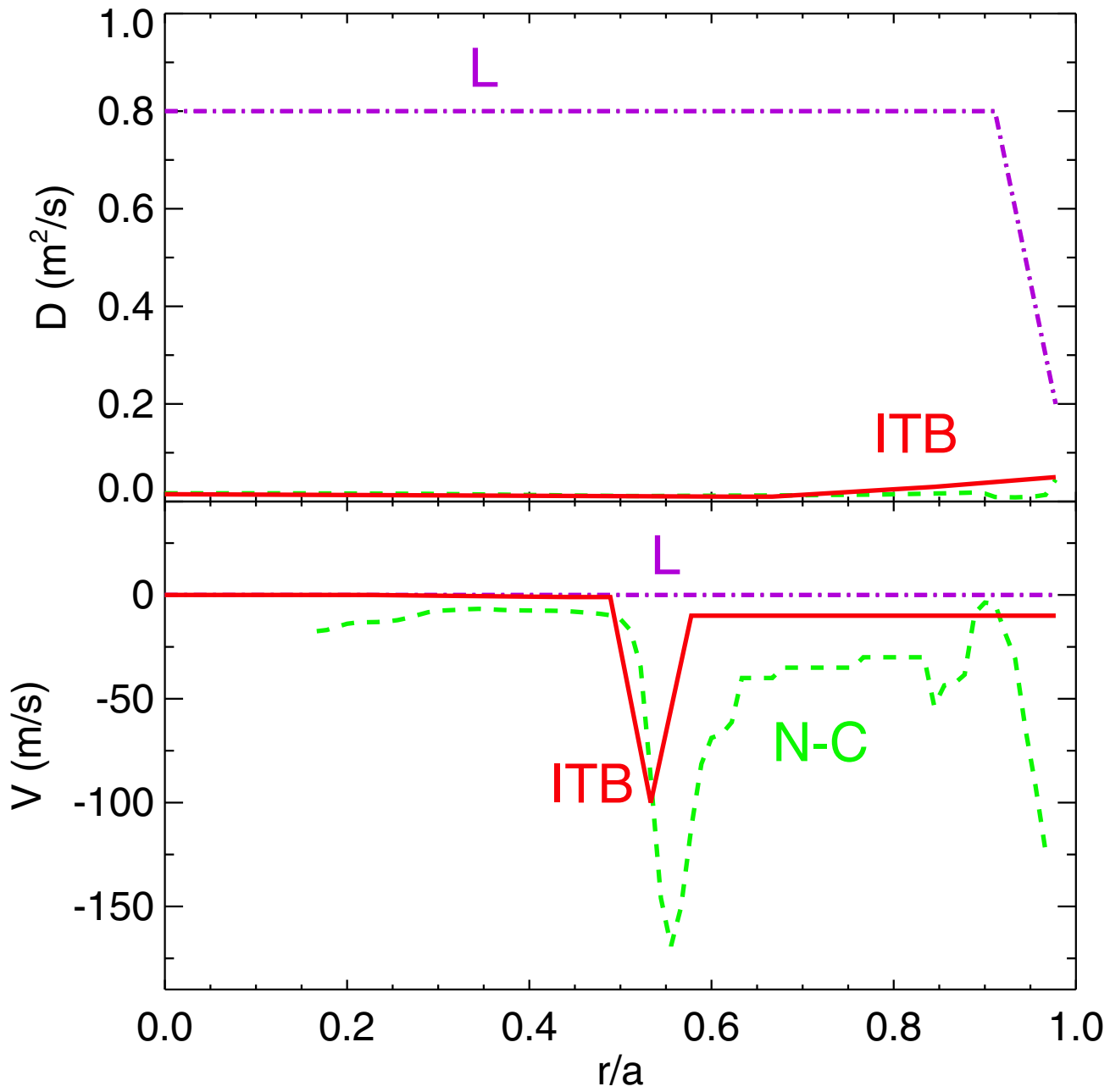


Figure 18

Ion BX ∇ B Drift Down

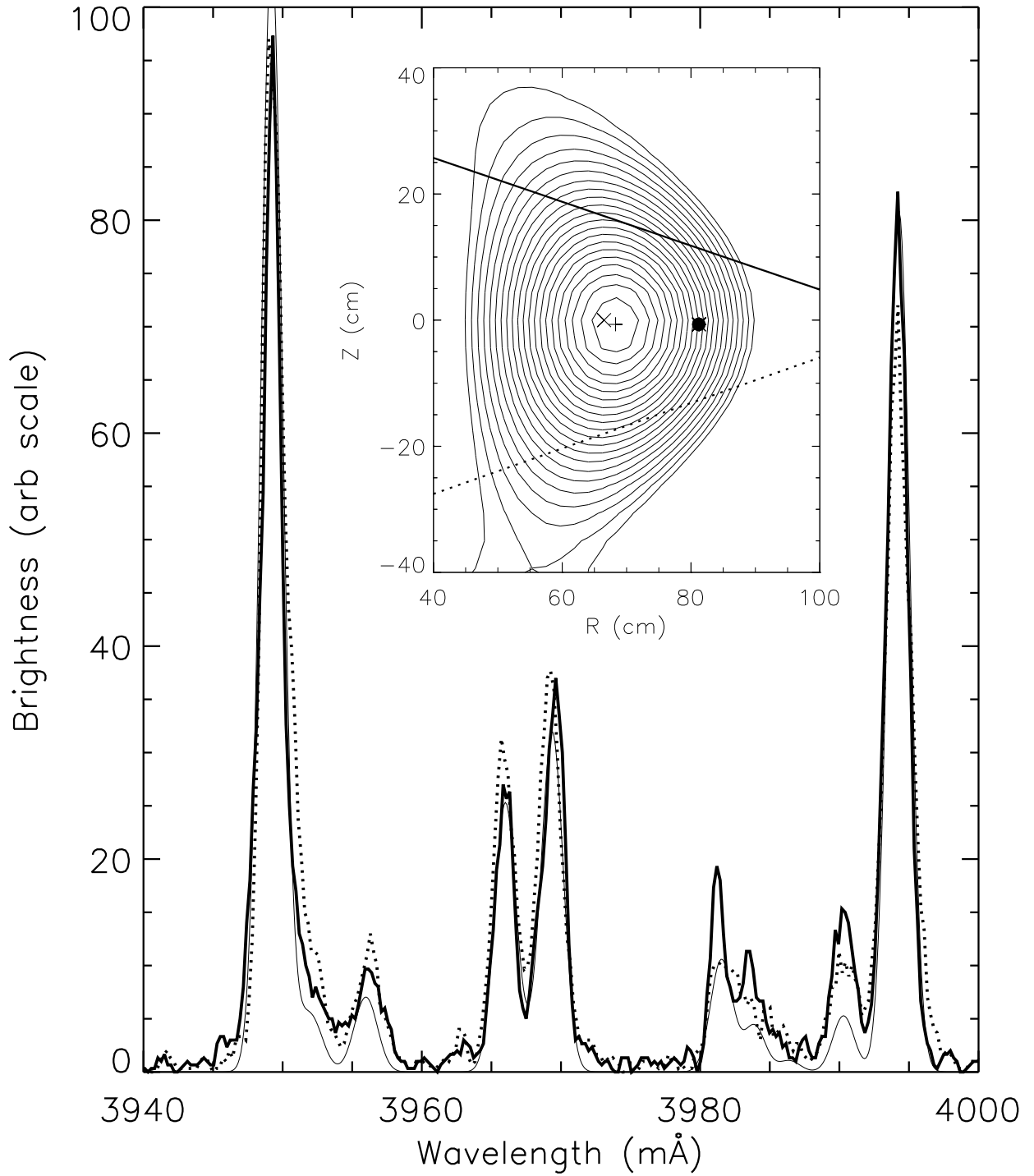


Figure 19

Ion BX ∇ B Drift Down

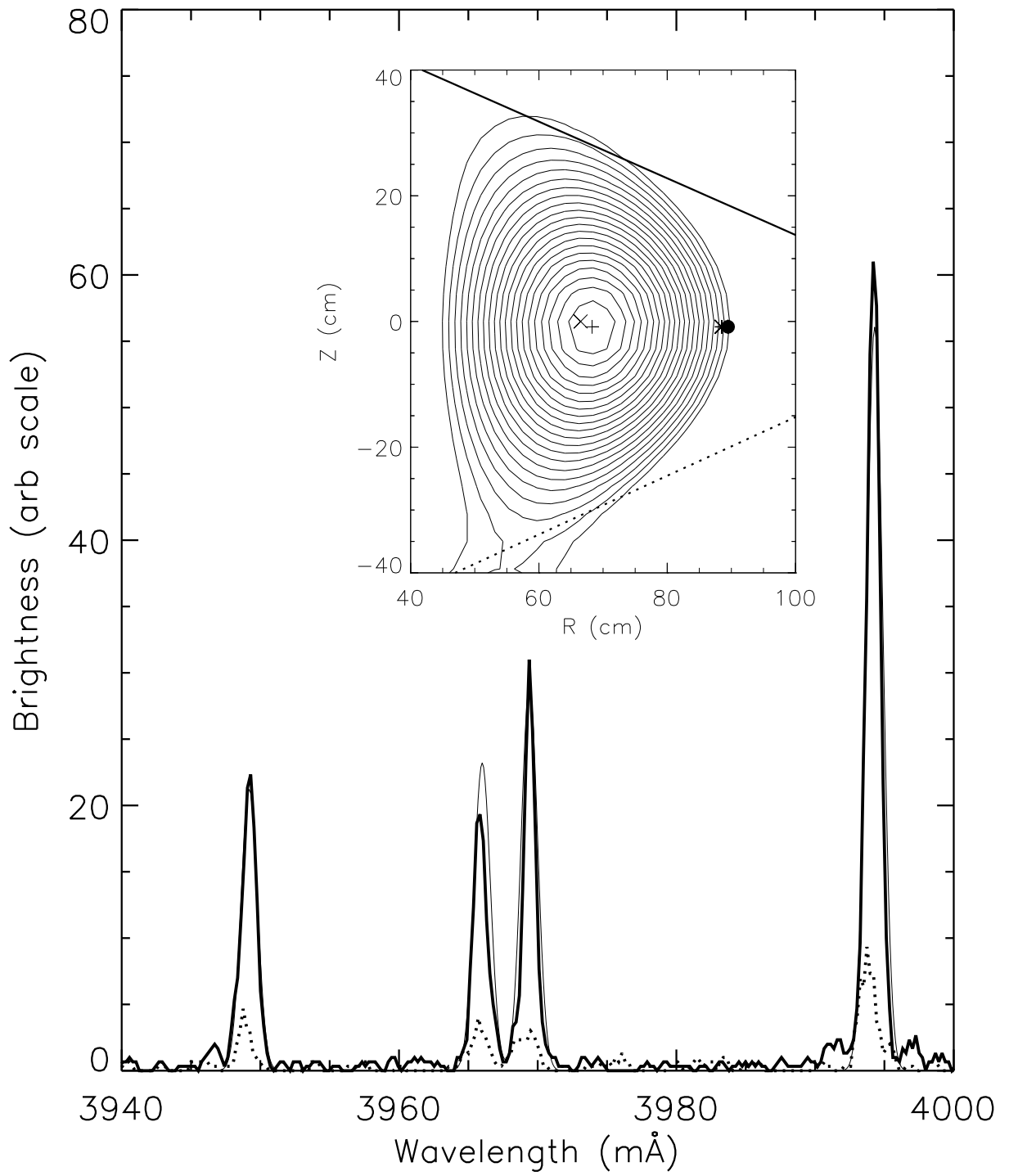


Figure 20

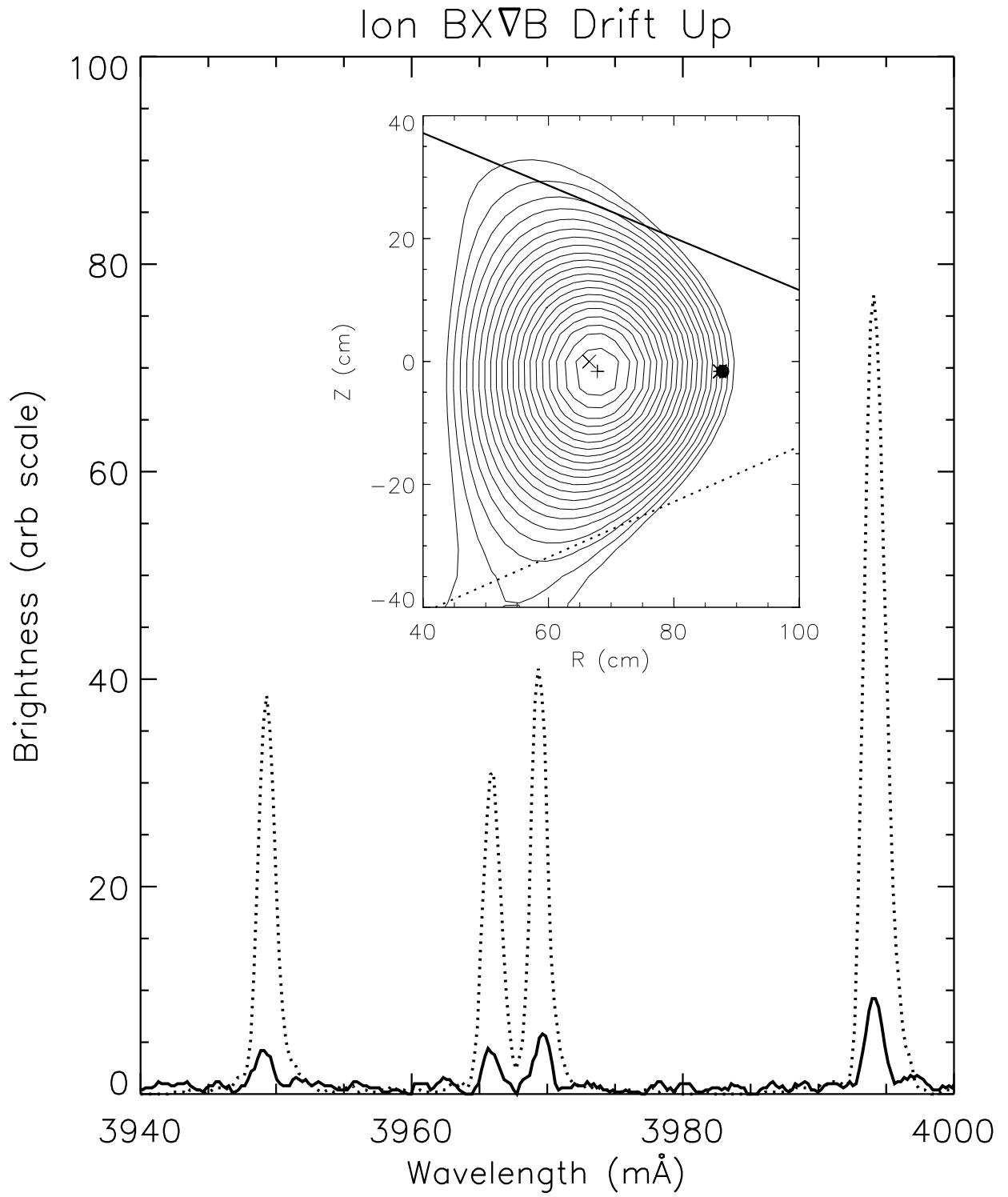


Figure 21

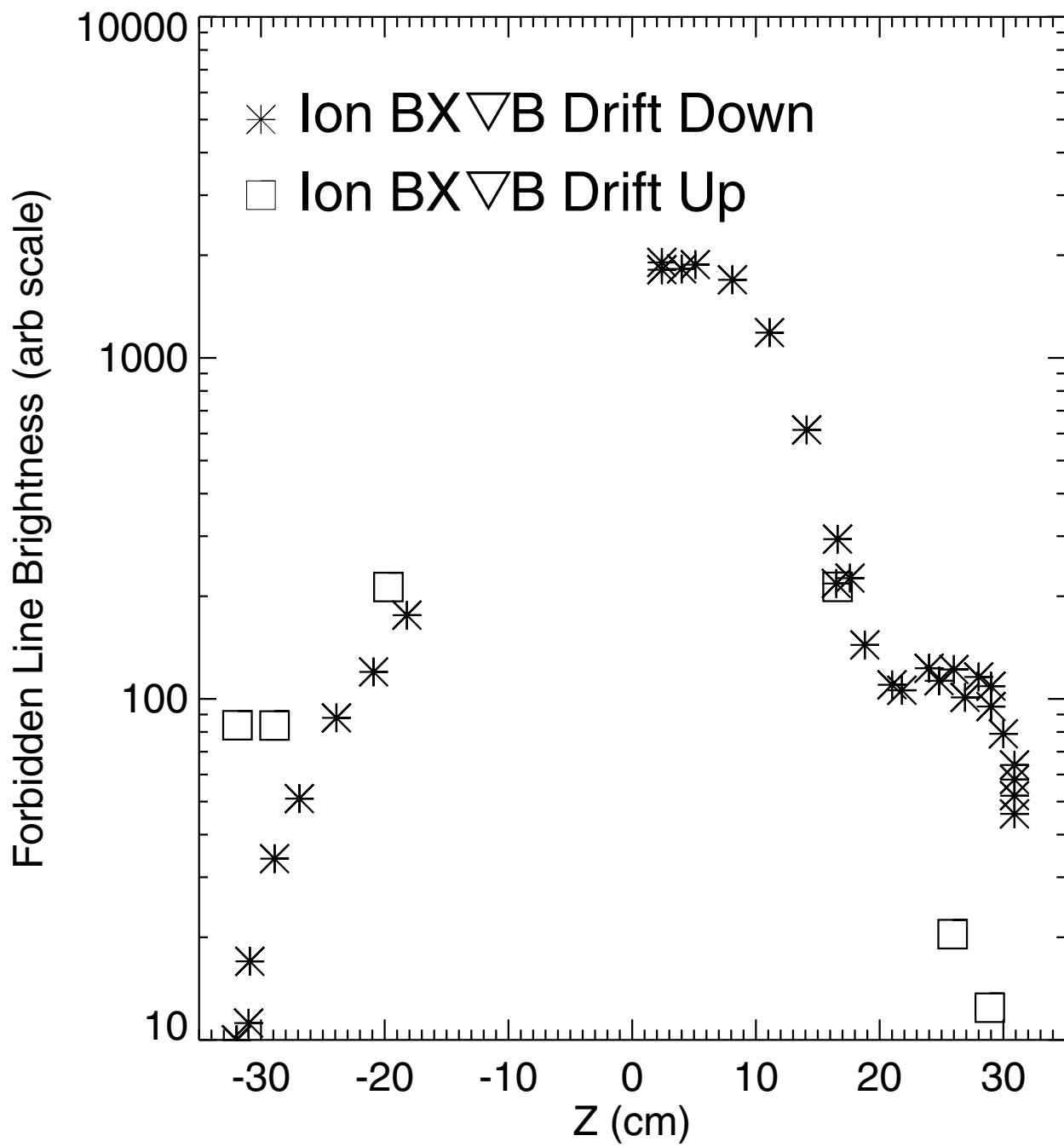


Figure 22